Engineering Structures 295 (2023) 116862

Contents lists available at ScienceDirect

Engineering Structures

journal homepage: www.elsevier.com/locate/engstruct

Precast segmental beams made of fibre-reinforced geopolymer concrete and FRP tendons against impact loads

Duong T. Tran [a], Thong M. Pham [b,*], Hong Hao [a,c,*], Ngoc San Ha [d], Nhi H. Vo [e], Wensu Chen [a]

[a] *Centre for Infrastructural Monitoring and Protection (CIMP), School of Civil and Mechanical Engineering, Curtin University, Kent St, Bentley, WA 6102, Australia*
[b] *UniSA STEM, University of South Australia, Mawson Lakes, SA 5095, Australia*
[c] *Earthquake Engineering Research and Test Center, Guangzhou University, Guangzhou 510006, China*
[d] *RMIT University, Melbourne, VIC 3001, Australia*
[e] *Kent, 191 St George's Terrace, Perth, WA 6000, Australia*

ARTICLE INFO

Keywords:
Prefabricated/precast segmental concrete beams (PSCBs)
Fibre-reinforced geopolymer concrete
Unbonded tendons
FRP
Impact behaviour/response
3D FE modelling

ABSTRACT

In the open literature, there is no investigation into the impact behaviour of prefabricated segmental concrete beams (PSCBs) cast with low CO_2-emission fibre-reinforced geopolymer concrete (GPC), reinforced with non-corrodible basalt fibre-reinforced polymer (BFRP) reinforcement, and post-tensioned with carbon FRP (CFRP) tendons. This research, hence, aims to close this existing gap of knowledge. The primary goals are to investigate the effect of dispersed fibres on the impact response of PSCBs and to compare the performance of CFRP versus steel tendons. The experimental results reveal that the PSCBs fail due to excessive joint openings that lead to concrete spalling and flying concrete debris. The inclusion of dispersed fibres in the concrete postpones crack development, reduces reinforcement strain, and effectively mitigates concrete spalling and stiffness degradation of the beams. While fibres show limited influence on the deflection response of PSCBs, as the deformation of segmental beams is predominantly governed by joint openings with no fibres bridging across the joints, they play a crucial role in preventing severe damage during impact events. The impact response of beams post-tensioned with CFRP tendons is analogous to those with steel tendons. Notably, both the CFRP tendon and BFRP reinforcement remain intact even when the beam fails under impact loads. This implies that CFRP tendons and BFRP reinforcement can be successfully employed in constructing durable and sustainable segmental GPC beams capable of withstanding impact loading. A high-fidelity numerical model of PSCBs made of GPC and FRP tendons and reinforcement subjected to impact loads is also developed, for the first time, to supplement the discussions of experimental findings.

1. Introduction

Precast/prefabricated segmental construction (PSC) is more advantageous than traditional site-cast monolithic construction in many aspects such as expedited construction time, decreased construction costs, reduced impacts on the environment and improved quality control. Structural resilience can be greatly enhanced with PSC as the functional restoration of segmental structures in case of damage can be done quickly by just replacing the damaged segments. Adopting PSC also promotes the use of advanced materials, e.g., ultra-high-performance concrete and fibre-reinforced concrete as these advanced materials sometimes warrant special handling with special equipment, careful blending and steam/heat curing, which often can only be achieved in prefabrication workshops or factories. Thus, precast segmental structures are regarded as one of the important structural forms in the next generation of design [1]. Recently, studies on prefabricated segmental concrete beams/girders (PSCBs) have been of keen interest [2–4]. Nonetheless, the contemporary understanding of the structural behaviour of PSCBs is mostly about their characteristics under static loading. There is a great gap in knowledge of the performance of segmental beams under extreme loading, e.g., impact and blast loads, which is now drawing strong attention from academia and industry [5–7]. This scarcity necessitates research studies to obtain insights into the response of PSCBs under impact loads.

Only two investigations of PSCBs subjected to impulsive (blast and impact) loads [8,9] can be found in the published literature. As reported

---

* Corresponding authors.

E-mail addresses: t.tran86@postgrad.curtin.edu.au (D.T. Tran), thong.pham@unisa.edu.au (T.M. Pham), hong.hao@curtin.edu.au (H. Hao), ngoc.san.ha@rmit.edu.au (N. San Ha), hoang.vo@kentplc.com (N.H. Vo), wensu.chen@curtin.edu.au (W. Chen).

https://doi.org/10.1016/j.engstruct.2023.116862
Received 8 May 2023; Received in revised form 6 August 2023; Accepted 3 September 2023

Table 1
GPC/FRGPC mixture.

Compositions	Unit	Quantity
Coarse aggregate (7 mm)	kg/m^3	1,100
Silica sand	kg/m^3	610
Fly ash (FA)	kg/m^3	340
Ground granulated blast furnace slag (GGBFS)	kg/m^3	60
NaOH solution (12 M)	kg/m^3	69
Na_2SiO_3 solution	kg/m^3	172
Alkaline activator / binder ratio		0.6
NaOH / Na_2SiO_3		2.5
Steel fibres (SF) 0.5% (for Beams S_SF0.5 and C_SF0.5)	kg/m^3	39.3
Recycled polypropylene fibres (PF) 0.5% (for Beam C_PF0.5)	kg/m^3	4.5
Recycled polypropylene fibres (PF) 1.0% (for Beam C_PF1)	kg/m^3	9
Micro SF 0.25% + PF 0.25% (for Beam C_S+PF05)	kg/m^3	19.6 + 2.3

in these two previous studies, the relative movement of adjoining segments (frictional slipping and opening of joints) in segmented structures under impulsive loading can absorb the imparted dynamic energy and thus decrease the induced stresses. As a result, under impulsive loads, the crack pattern and failure mode of the segmental structures are very different from their monolithic counterparts, and the damage inflicted on the former is normally less severe than on the latter as observed in the previous experimental and numerical studies [8–12]. For example, in a recent experimental investigation under impact loading [9], it was found that cracks were predominantly localised in the vicinity of joints in PSCBs because of joint openings. Excessive joint openings led to concrete spalling near the joint and the beam failure. By contrast, flexural or flexure-shear cracks appeared in the reference monolithic beams because of high impact-induced internal forces. The failure of monolithic beams resulted from the development of flexure-shear cracks, leading to the rupture of reinforcing bars. In addition, owing to the energy absorption mechanism associated with joint openings, in some cases, segmental structures showed greater resistance against dynamic loading than their monolithic counterparts [8,10].

As the world is making every endeavour to achieve net zero emissions to prevent catastrophic climate repercussions resulting from man-made greenhouse gas emissions, using low-carbon/low-emission/green cementitious materials instead of ordinary Portland cement concrete (OPC) is considered one of the promising solutions [13]. This is because Portland cement production emits a significant amount of carbon dioxide (CO_2) - the major greenhouse gas. Geopolymer concrete (GPC) or alkali-activated concrete is widely recognised as an auspicious sustainable material due to containing no Portland clinker in its constituents and hence up to 90% of construction carbon footprint can be eliminated [14]. Geopolymer cement is made by the geopolymerisation between alkaline activating solutions and by-product-based aluminosilicates [15] such as ground granulated blast-furnace slag (GGBFS) and fly ash [16]. Reusing these by-products in producing GPC brings additional environmental advantages. Besides its eco-friendly feature, GPC has high early strength and resistance against fire and acid [16–18] and can be made under ambient conditions with sufficient strength for structural applications [16]. GPC has been found to offer PSCBs a similar impact performance as OPC, as reported in a previous study [9]. Despite its various merits, GPC is inherently brittle and thus GPC structures typically have inferior cracking resistance and a brittle failure compared to OPC counterparts [19,20], impeding the adoption of GPC. To overcome this impediment, dispersed fibres can be incorporated into the concrete to enhance its cracking resistances, flexural strength, ductility and toughness [21–24]. The bending and shear resistances and ductility of monolithic fibre-reinforced GPC (FRGPC) beams under static loads were reported to increase due to the fibres [20]. Fibres also helped control crack formation and development and decrease the maximum and residual deflection of monolithic FRGPC beams under impact loads [25]. Nonetheless, the effect of dispersed fibres on the impact performance of segmental GPC beams has not been investigated yet.

On the other hand, corrosion of steel reinforcement/tendons causes cracks and compromises the stiffness, serviceability and loading resistance of conventional concrete structures [26,27]. This problem is even worse in segmental structures because tendons are the primary element resisting tensile stresses at the segment joints and they are less protected against the environment, especially for segmental structures with dry joints. Therefore, adopting non-corrodible fibre-reinforced polymer (FRP) tendons and/or reinforcing bars to construct structures is an effective solution for this corrosion-related problem. GPC or FRGPC structures prestressed with FRP tendons and/or reinforced with FRP rods can be regarded as durable and sustainable, and thus are more and more adopted [25,28–32]. No research studies have, however, been reported to examine the response of FRGPC segmental beams prestressed and reinforced with FRP composites in the literature yet.

This study is a continuation of the authors' previous research efforts [8,9], which investigated the blast and impact responses of PSCBs made of plain OPC and/or GPC in comparison with their monolithic counterparts. This current paper aims to experimentally investigate the impact behaviour of PSCBs constructed with fibre-reinforced geopolymer concrete (FRGPC), prestressed with CFRP/steel tendons, and reinforced with BFRP rods. The experimental program consisted of six dry key-jointed PSCBs post-tensioned with unbonded tendons. The primary goals are to examine the effect of fibres on the impact behaviour of PSCBs and the performance of CFRP versus steel tendons. Additionally, this paper develops a three-dimensional high-fidelity finite element model of segmental beams made with GPC and FRP tendons and reinforcement for the first time. The numerical simulation is carried out to supplement the observations and discussions of the experimental findings.

2. Test program

2.1. Materials

Ambient-cured geopolymer concrete (GPC) with a density of 2,351 kg/m^3 was used in this study. The concrete mix design is presented in Table 1. Crushed stones and silica sand respectively served as coarse and fine aggregates of the GPC. The aluminosilicate precursors for the GPC were ground granulated blast furnace slag (GGBFS) and low-calcium fly ash (FA), and their chemical compositions were reported in detail in [9]. A blend of D-grade sodium silicate (Na_2SiO_3) and 12 M sodium hydroxide (NaOH) solutions was the alkaline activating solution (Aa) of the GPC. The D-grade Na_2SiO_3 solution compositions included Na_2O (14.7%), SiO_2 (29.4%) and H_2O (55.9%). One litre of 12 M NaOH solution was produced by dissolving 480 g of solid NaOH (40 g/mol) in H_2O.

Three different types of fibres were adopted to make fibre-reinforced GPC (FRGPC), namely macro steel fibres (SF), macro recycled polypropylene fibres (PF), and micro steel fibres, as shown in Fig. 1. Table 2 shows the size and properties of these fibres. The macro SF were Dramix 3D hooked-end steel fibres [33], while the macro recycled PF were BarChip R50 continuously embossed fibres supplied by BarChip Australia [34]. The micro SF were the straight copper-coated steel fibres [35] which are corrosion resistant. Macro SF were chosen due to their excellent mechanical properties and recognised effectiveness in improving the performance of structures. Marco recycled PF were adopted because they are eco-friendly, chemical-resistant, lightweight, structurally effective and an ideal solution to the corrosion associated

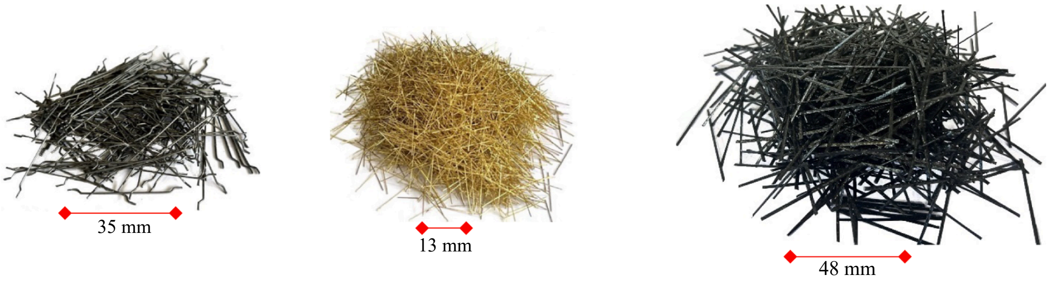

(a) Macro steel fibres (SF) **(b)** Micro steel fibres (SF) **(c)** Macro recycled polypropylene fibres (PF)

(d) Steel tendon (nominal Ø12.7 mm)

(e) CFRP tendon (Ø12.6 mm)

(f) Longitudinal BFRP bar (Ø6 mm)

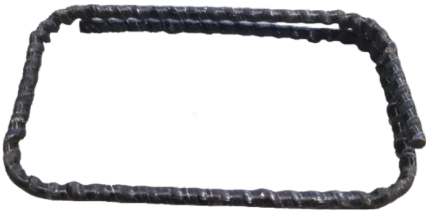

(g) BFRP stirrup (Ø6 mm)

Fig. 1. Materials adopted in this study.

Table 2
Properties of fibres.

Fibres	Appearance	Density kg/m^3	Length (L) mm	Diameter (D) mm	Aspect ratio (L/D)	Tensile strength MPa	Young's modulus GPa
Macro steel fibres	Bright, hooked-end	7,850	35	0.55	64	1,345	210
Macro recycled polypropylene fibres	Continuously embossed	900	48	–	–	610	10
Micro steel fibres	Copper-coated, straight	7,850	13	0.2	65	2,300	200

Table 3
Beam specification.

Beam	Description	V_f	f_c MPa	$f_{c,spl}$ MPa	Tendon material	F_{pe} kN	b mm	h mm	L_O mm	L mm
C_0	No fibres	0	53.0	5.5	CFRP	69	120	180	1,550	1,400
S_SF05	Macro steel fibres (SF)	0.5%	52.4	7.4	Steel	62				
C_SF05	Macro SF	0.5%	52.4	7.4	CFRP	57				
C_PF05	Macro recycled polypropylene fibres (PF)	0.5%	50.0	6.5	CFRP	60				
C_PF1	Macro PF	1.0%	51.1	7.1	CFRP	55				
C_S+PF05	Hybrid micro SF + macro PF	0.5%	50.8	7.0	CFRP	59				

Note: V_f is the volume fraction of fibres; f_c and $f_{c,spl}$ are the compressive and splitting tensile strengths of concrete cylinders, respectively; F_{pe} is the effective post-tensioning force; b and h are respectively the cross-sectional width and height of the specimen; and L_O and L are the total length and effective span of the specimen, respectively.

with steel. Meanwhile, a single type of fibre which can improve the performance of structures in all aspects (ductility, strength and durability) does not exist. Hence, the hybridisation of different kinds of fibres, e.g., micro and macro fibres, is adopted to utilise synergy benefits between the individual kind of fibres. Micro fibres are effective in bridging and arresting microcracks and reducing shrinkage cracks while macro fibres are beneficial to controlling macrocracks [23,36,37]. Thus the cracking, post-cracking performance and toughness of concrete can be greatly enhanced by using hybrid micro and macro fibres. In this study, hybrid fibres of micro corrosion-resistant SF and macro recycled PF were adopted. The volume of dispersed fibres was chosen to be less than 1.0% based on the recommendations of previous experimental studies [22,30] to ensure the constructability of the structure when considering the low workability of GPC. The mixing process of fibres was done in accordance with the guidelines of the fibre manufacturers [38,39] to ensure the uniform distribution of fibres in concrete. Specifically, after adding all fibres, the concrete was mixed with a drum speed greater than 12 rpm in one minute/m^3 concrete and not less than five minutes. The uniform distribution of fibres in concrete was also ensured based on observation during the mixing process.

The GPC's mechanical properties were experimentally determined based on Australian standards AS 1012.9:2014 [40] and AS 1012.8.1:2014 [41]. The uniaxial compressive strength of concrete (f_c) was determined from the test data of three cylinders with a diameter of 100 mm and a height of 200 mm, and its indirect tensile strength was acquired based on three cylinders with 150 mm diameter and 300 mm height. The average GPC compressive strength and indirect tensile strength of each beam (aged 144 days) were tabulated in Table 3. The dispersed fibres only had a negligible effect on the compressive strength of concrete as reported in previous studies [22,42]. However, the concrete tensile strength was significantly increased with the incorporation of the fibres. With a fibre volume fraction of 0.5%, the macro steel fibres (SF) were the most effective in improving the splitting tensile strength of the concrete at 34%, followed by the hybrid micro steel and macro recycled polypropylene fibres (S + PF) at 27% and the macro recycled polypropylene fibres (PF) at 18% (Table 3). The splitting tensile strength

Table 4
Properties of tendons and reinforcement.

Materials	Density kg/m^3	Nominal diameter mm	Area mm^2	Tensile strength MPa	Nominal yield strength MPa	Young's modulus GPa	Rupture strain
Steel tendons	7,850	12.7	100	1,860	1,674	196	5.0%
CFRP tendons	1,500	12.6	125	2,450	–	145	1.7%
BFRP reinforcing bars	1,950	6	28	1,200	–	55	2.1%

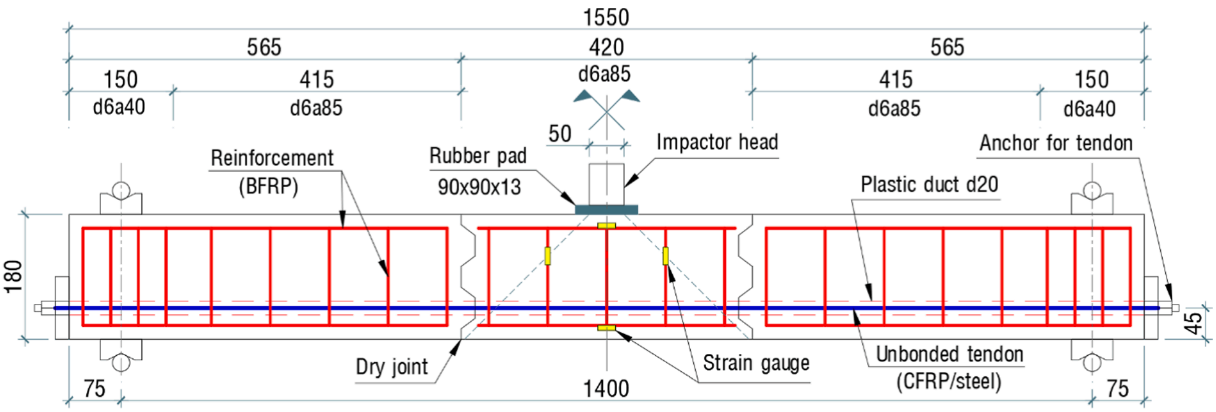

a) Segmental beam

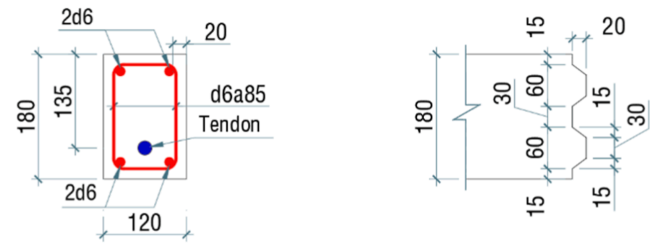

b) Typical cross-section c) Detail of shear key

Fig. 2. Design of the tested beam (dimensions in mm).

of the concrete increased by 9% when increasing the fibre dosage of macro PF from 0.5% to 1.0% (Table 3).

Regarding the prestressing tendons, steel 7-wire strands (Fig. 1**d**) and carbon fibre-reinforced polymer (CFRP) rods (Fig. 1**e**) were adopted. The basalt fibre-reinforced polymer (BFRP) bars were used for longitudinal reinforcement (Fig. 1**f**) and stirrups (Fig. 1**g**). The mechanical properties of the tendons and the reinforcement are tabulated in Table 4. The mechanical properties of steel tendons are guaranteed by the manufacturer to meet the requirements of ASTM A416/A416M-18 [43]. The mechanical properties of CFRP tendons and BFRP bars were provided by the manufacturers [44,45].

2.2. *Specimen design*

The test program was conducted on six PSCBs, including one GPC and four FRGPC beams post-tensioned with CFRP tendons and one FRGPC beam post-tensioned with conventional steel tendons (see Table 3). The specimen designation comprises two components in which the material of tendons is indicated in the first component ("S" for steel tendons and "C" for CFRP tendons). The type and volume fraction of fibres are shown in the last component, i.e., "SF0.5" for 0.5% of macro steel fibres (SF), "PF0.5" and "PF1" respectively for 0.5% and 1.0% of macro recycled polypropylene fibres (PF), and "S+PF0.5" for 0.25% of micro SF + 0.25% of macro recycled PF. For instance, Beam C_SF05 is the segmental beam prestressed with CFRP tendons and cast with GPC with 0.5% macro steel fibres.

The dimensions of the tested beams were 120 × 180 × 1,550 mm with an effective span of 1,400 mm as illustrated in Fig. 2. Previous experimental investigations [9,46,47] also adopted similar dimensions. The span-to-depth ratio (L/d_p) of the tested beams was 10.4, meaning that the flexural behaviour was expected to govern the beam response [48]. Unbonded tendons were chosen in post-tensioning the beams because they expedite the construction process, resulting in reduced construction costs and convenience in maintenance and replacement. It is, however, noted that there is no strain compatibility between the unbonded tendons and the adjacent concrete and the post-tensioning forces are transmitted to the structural member only through the tendon anchors [49–51]. The test beams were designed with Class U (uncracked) following ACI 318–19 [52] as also adopted in previous experimental investigations [53–55]. Additionally, the segmental beams were designed to have dry joints which have multiple shear keys (Fig. 2), as commonly used in practice. The popular isosceles trapezoid shape was chosen for the shear keys [2,4]. The shear keys had an angle of their inclined faces greater than 55° and a depth-to-length ratio higher than 0.13 for the highest loading resistance [56,57]. AASHTO [58] was adopted to design the shear-keyed joint whose static shear resistance was higher compared to the beam's shear resistance to avert the shear failure of the joint.

For the auxiliary reinforcement, both the bottom and top longitudinal reinforcement were two Ø6-mm BFRP rods with a concrete cover of 20 mm, as shown in Fig. 2. The ratio of tensile longitudinal reinforcement of the beam was 0.3%, satisfying the minimum ratio requirement according to ACI 440.1R-15 [59]. Two-legged BFRP bars of Ø6 in diameter served as the stirrups of the beam. The stirrups were spaced at 85 mm with a stirrup ratio of 0.55% to have the beam's static shear resistance three times greater than its static bending resistance to

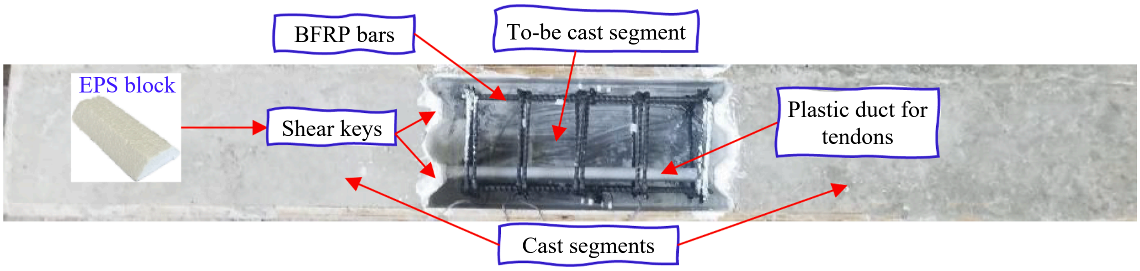

Fig. 3. Segmental beam casting.

avoid shear failure. The static bending and shear resistances were calculated according to ACI 440.1R-15 [59] and ACI 318–19 [52]. It is noted that 40 mm of stirrup spacing was used in the region of 150 mm on the beam ends (Fig. 2) to avoid potential localised damage caused by prestressing forces.

2.3. Specimen fabrication and test setup

The beam specimens were fabricated in laboratory conditions. To divide the segments of the beams, plywood plates were used on which expanded polystyrene (EPS) foam blocks with the shape of isosceles trapezoids were bonded to create a mould for the shear keys (see Fig. 3). The hole for the prestressing tendons was created using a plastic duct of 20 mm in diameter. The match-casting method was used to fabricate the segmental beams where segments of the beam were fabricated alternately. For instance, both the end segments were fabricated first, and later they were used as moulds for constructing the last segment, as shown in Fig. 3. The last casting was done five days after the first casting. Adopting the match-casting technique enables a good matching between the male and female shear keys (mortise and tenon) of the adjoining segments. The specimens were left in laboratory conditions for at least 28 days before the post-tensioning and testing.

The beam was secured vertically in a rigid steel frame with a simply supported condition, as shown in Fig. 4**a** and **b**. The support system consisted of rollers, steel plates, bolts and clamp plates. The top and bottom clamp plates were fixed together using four bolts of Ø18 mm (Fig. 4**a**). The beam was post-tensioned using the jacking system shown in Fig. 4**c**. The force in unbonded tendons can be assumed unchanged along their entire length between the tendon anchors; accordingly, the tendon force was measured using a barrel load cell placed at one end of the tendon between the concrete beam and tendon anchor, as shown in Fig. 4**a**. The tendon force was automatically recorded throughout the entire prestressing and impact testing events. The effective prestressing force (F_{pe}) is tabulated in Table 3. Even though rigorous efforts and care were exerted in the prestressing, the F_{pe} of Beam C_0 was unexpectedly 17% on average higher than the F_{pe} of the other beams (Table 3). After prestressing, the bolts at each support were tightened with a total force of 13 kN immediately before the impact test.

The beam was struck by a pendulum mass of about 560 kg at mid-span with three increased impact loads. The pendulum head was made of a steel cylinder of Ø50 mm having a curved surface with a curvature radius of 250 mm. A steel square hollow section (SHS) of 75 × 75 × 6 mm was used to make the pendulum arm (2,044 mm in length) which was welded to a hinge support on the rigid steel frame (Fig. 4**b**). The impact loads were generated by releasing the pendulum mass from the desired release angle (θ in Fig. 4**b**), i.e., 5°, 20° and 40°. The release angle was determined using a protractor with an accuracy of ± 1°. The velocity of the pendulum hitting the beam was determined by the image processing of the high-speed camera records. The beam was left resting for about five minutes after each impact load. To minimise inertial oscillations of the specimen [60] and produce a soft contact condition of impact, a rubber pad (90 × 90 × 13 mm) was used as an interlayer between the beam and pendulum. The rubber pad was made of natural rubber with a hardness of 60 IRHD Duro ± 5 (Granor Rubber & Engineering, Australia) and was replaced with a new one to have a similar condition of contact for each impact test.

The footage of the impact test was captured using an ultrahigh-speed camera with a frame rate of 20,000 (Fig. 4**b**). Track points were glued to the pendulum and specimen (Fig. 4**a**) for post-processing using the digital image correlation (DIC) method to determine the specimen displacement and the pendulum velocity. A load cell embedded in the pendulum head was employed to record the impact force while 200-kN load cells were used to measure the prestressing and reaction forces. The reinforcement strain was measured by using strain gauges (SGs) whose positions are shown in Fig. 2. A data acquisition system was used to acquire the displacement, forces and strain of the specimen at 10,000 Hz. This sampling rate is sufficient for this slow-velocity impact test as recommended by [61].

Regarding the anchor of the tendons, the conventional anchor involving barrels and wedges was used as shown in Fig. 4**c**. However, this conventional anchor was not applicable to the CFRP tendons since they were brittle and had low compressive and shear strengths. Therefore, a special friction-based anchor shown in Fig. 4**d** was designed and manufactured for the CFRP tendons in this study. This anchor for the CFRP tendons included a gripping cylinder, high-strength M12 hex socket screws and an aluminium sleeve with a thickness of 1.0 mm. This aluminium sleeve served as a soft interlayer between the tendon and the anchor to avoid stress concentration and distribute the gripping force uniformly to the tendon. A torque of 90 Nm was applied at each screw. This anchor was reusable and capable of holding the CFRP tendons in place until rupture.

3. Experimental results and discussions

The experimental results showed that no visible damage or cracks were observed in all the tested beams during the impact test with a release angle of 5° associated with the recorded impact velocity (V_i) of roughly 0.4 m/s. This impact loading aimed to evaluate the elastic behaviour of the beam. In this study, only the beam behaviour in the following impact loads produced by the release angles of 20° and 40° with V_i respectively of 1.52 m/s and 3.09 m/s are reported and examined.

3.1. Behaviour under 20° impact test ($V_i = 1.52$ m/s)

Table 5 summarises the impact performance of all the tested beams, while Fig. 5 displays the typical response of the displacement and impact force of the specimen under the 20° impact ($V_i = 1.52$ m/s). The beam behaviour can be separated into three different stages of displacement, i.e., Stage 1 (ascending), Stage 2 (descending) and Stage 3 (free vibration). The beam started from rest and rose to its maximum displacement as the pendulum struck the specimen in Stage 1. The impact force also peaked in this stage. In Stage 2, the beam rebounded to its initial position and the impact force declined to nil. In Stage 3, the pendulum and beam detached from each other, and the beam vibrated freely.

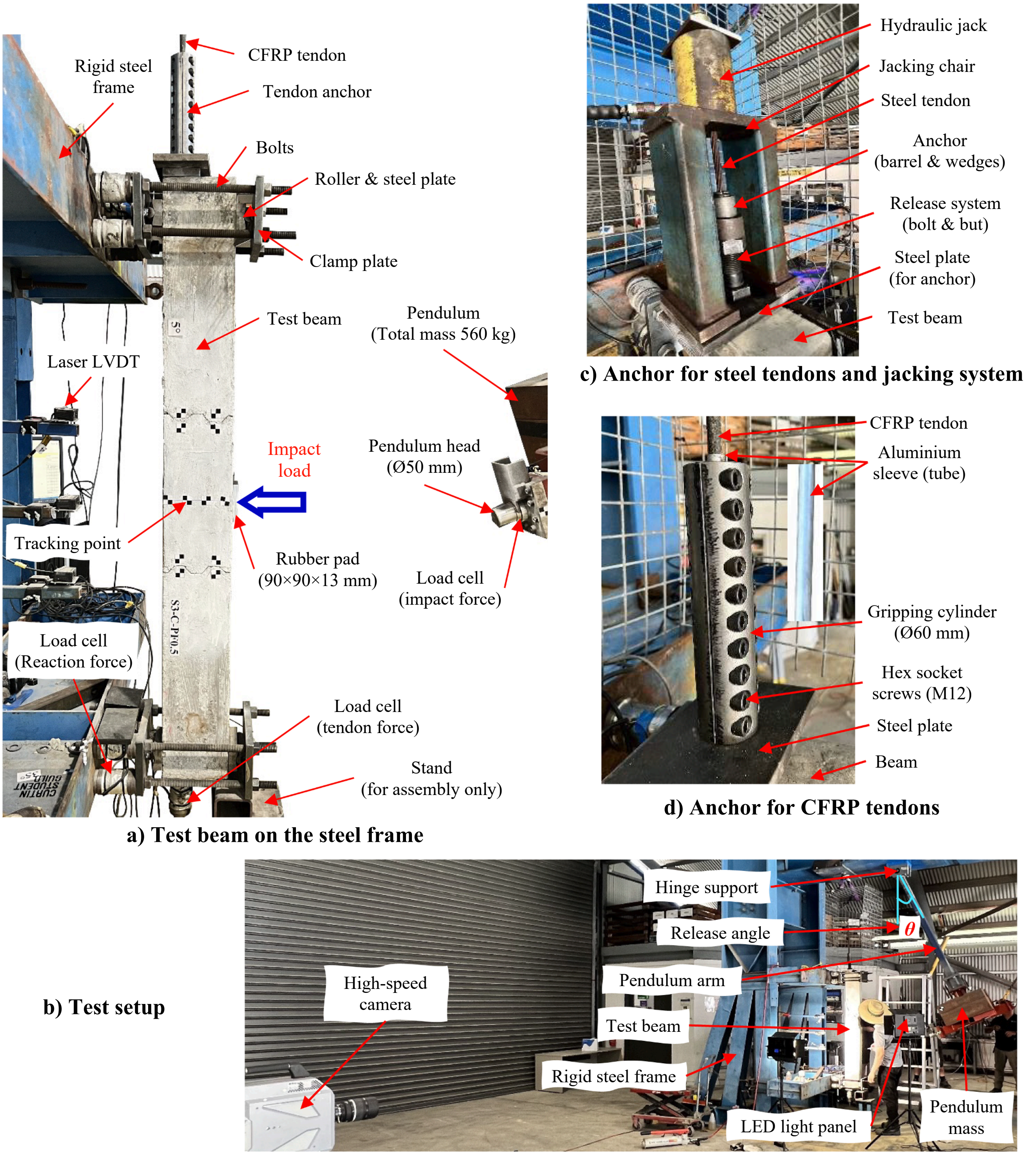

a) Test beam on the steel frame

b) Test setup

c) Anchor for steel tendons and jacking system

d) Anchor for CFRP tendons

Fig. 4. Experimental setup and tendon anchors.

3.1.1. *Damage pattern under 20° impact test ($V_i = 1.52$ m/s)*

Fig. 6 displays the crack morphology of the specimens under the 20° impact ($V_i = 1.52$ m/s). The camera footage of Beam C_SF05 under the 20° impact was lost and hence no photo of the damage pattern of this beam was available. In general, the impact-induced damage mostly occurred in Stage 1. Firstly, from the observation of the footage of the PSCB without fibres (Beam C_0), the first crack was flexural (transverse to the axis of the beam) and emerged from the midspan soffit of the beam at around 8 ms after the collision with the pendulum (see Fig. 6**a**). High bending moments at the beam midspan caused this crack. As the impact load caused the segment joint openings (Fig. 6**a**), the shear keys of adjacent segments were compressed to one another, leading to stress concentration, as demonstrated in Fig. 7 from the numerical simulation. It is noted that the numerical model is presented later but its results are shown here to support the discussion of the experimental observation. Consequently, longitudinal cracks emerged from the corners of the joint's shear keys near the striking point at about 9 ms (see Fig. 6**a**). Section Appendix presents the development of the three-dimensional (3D) high-fidelity finite element (FE) model of segmental beams made of geopolymer concrete, BFRP reinforcement and prestressed with CFRP tendons – the first FE model of this type of beam in the literature.

Regarding the other beams with fibres, as compared to Beam C_0, the

Table 5
20° impact test results (V_i = 1.52 m/s).

Beam	V_i m/s	P_m kN	P_{pa} kN	t_d ms	I kNs	R_m kN	δ_m mm	δ_r mm	$F_{p,i}$ kN	$F_{p,m}$ kN	$F_{p,r}$ kN
C_0	1.54	63	41	47	1.44	26	8.8	0.2	69	95	68
S_SF05	1.46	51	46	51	1.34	24	9.2	0.3	62	83	59
C_SF05	–	56	41	50	1.41	25	9.0	0.3	57	83	57
C_PF05	1.53	66	44	49	1.41	26	9.0	0.1	60	80	60
C_PF1	1.50	52	46	52	1.42	25	9.3	0.2	55	78	54
C_S+PF05	1.56	56	46	50	1.45	26	10.1	0.2	59	89	59

Note: "-" means data lost; V_i is the measured impact velocity; P_m and P_{pa} are the maximum and the average of the plateau of impact force (see Fig. 8), respectively; R_m is the maximum reaction force; t_d and I are, respectively, the duration and impulse of impact load; δ_m and δ_r are the beam's peak and residual displacement at midspan, respectively; and $F_{p,i}$, $F_{p,m}$ and $F_{p,r}$ are, respectively, the initial, maximum, and residual tendon forces.

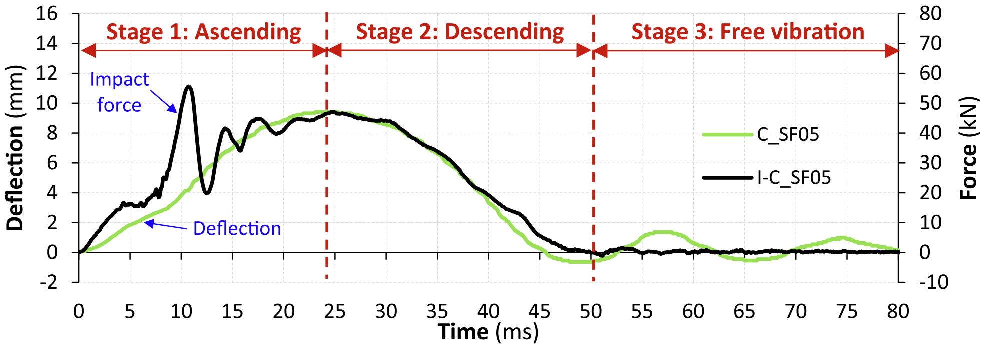

Fig. 5. Stage classification under 20° impact (V_i = 1.52 m/s).

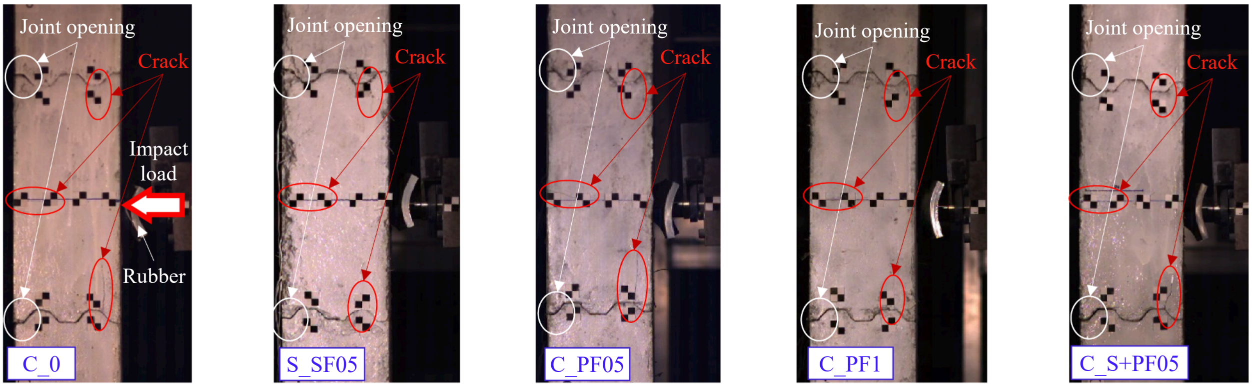

a) At the max displacement

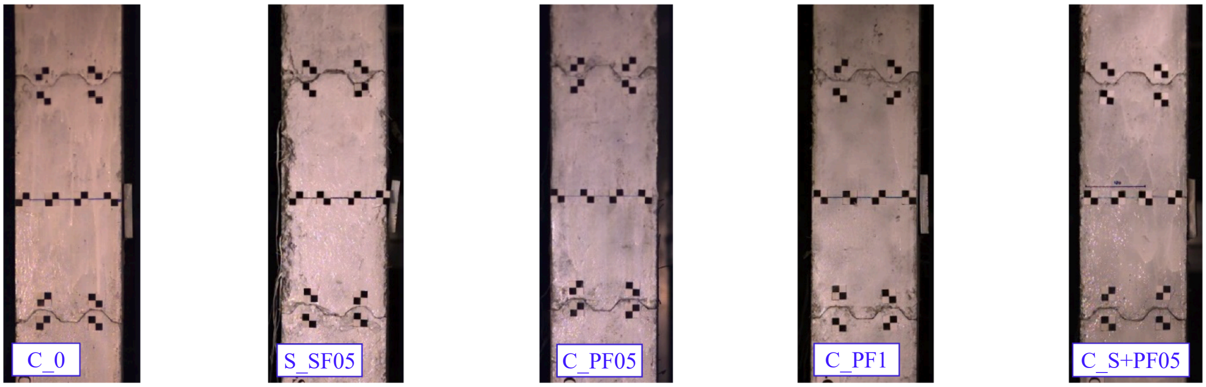

b) After 20° impact

Fig. 6. Damage pattern under 20° impact (V_i = 1.52 m/s).

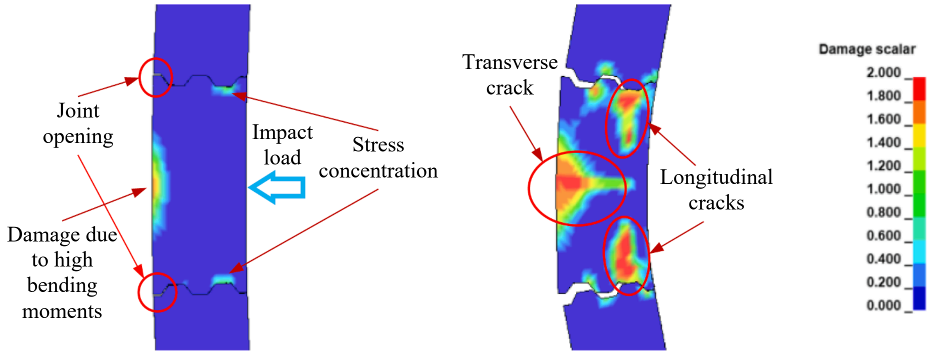

a) At 4 ms **b) At 10 ms**

Fig. 7. Joint opening and damage of simulated Beam C_0.

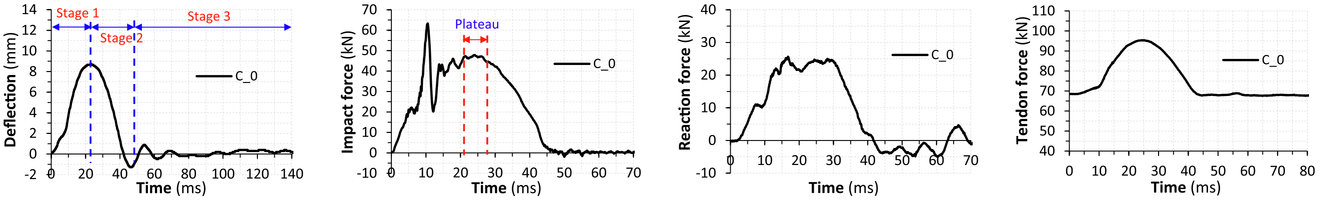

a) Displacement (no fibres) **b)** Impact load (no fibres) **c)** Reaction force (no fibres) **d)** Tendon force (no fibres)

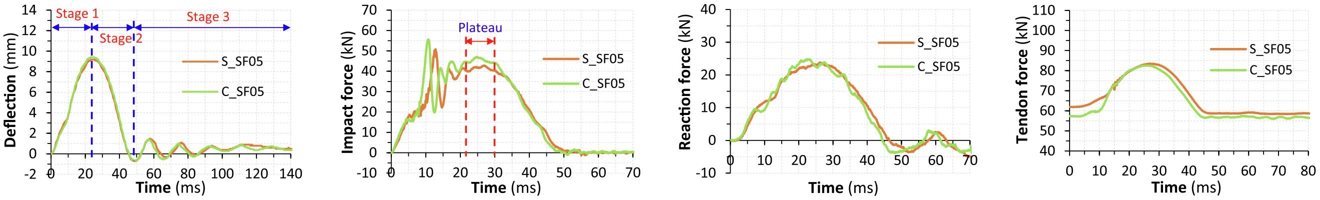

e) Displacement (steel fibres) **f)** Impact load (steel fibres) **g)** Reaction force (steel fibres) **h)** Tendon force (steel fibres)

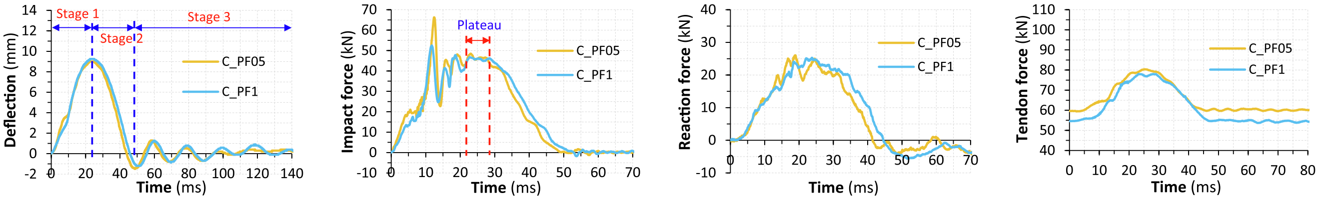

i) Displacement (polypropylene fibres) **j)** Impact load (polypropylene fibres) **k)** Reaction force (polypropylene fibres) **l)** Tendon force (polypropylene fibres)

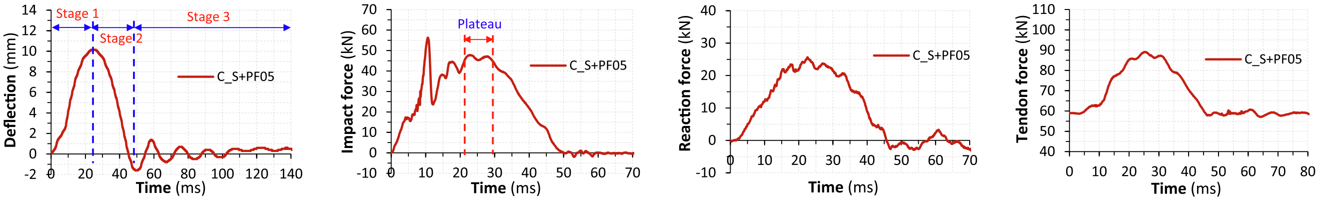

m) Displacement (hybrid fibres) **n)** Impact load (hybrid fibres) **o)** Reaction force (hybrid fibres) **p)** Tendon force (hybrid fibres)

Fig. 8. Responses of displacement, impact load, reaction force, and tendon force under the 20° impact ($V_i = 1.52$ m/s).

Table 6
40° impact test results ($V_i = 3.09$ m/s).

Beam	V_i m/s	P_m kN	P_{pa} kN	t_d ms	I kNs	R_m kN	δ_m mm	δ_r mm	$F_{p,i}$ kN	$F_{p,m}$ kN	$F_{p,r}$ kN
C_0	3.12	122	60	62	2.63	51	34	0.1	68	162	62
S_SF05	3.10	102	56	71	2.61	53	41	0.2	59	143	35
C_SF05	3.09	119	66	61	2.76	55	35	0.3	57	148	50
C_PF05	3.03	101	69	64	2.89	55	37	−0.2	60	150	58
C_PF1	3.05	107	72	64	2.92	58	39	−0.3	54	148	52
C_S+PF05	3.11	111	69	66	2.90	52	40	−0.3	59	168	53

Note: V_i is the measured impact velocity; P_m and P_{pa} are the maximum and the average of the plateau of impact force (see Fig. 12), respectively; R_m is the maximum reaction force; t_d and I are, respectively, the duration and impulse of impact load; δ_m and δ_r are the beam's peak and residual displacement at midspan, respectively; and $F_{p,i}$, $F_{p,m}$ and $F_{p,r}$ are, respectively, the initial, maximum, and residual tendon forces.

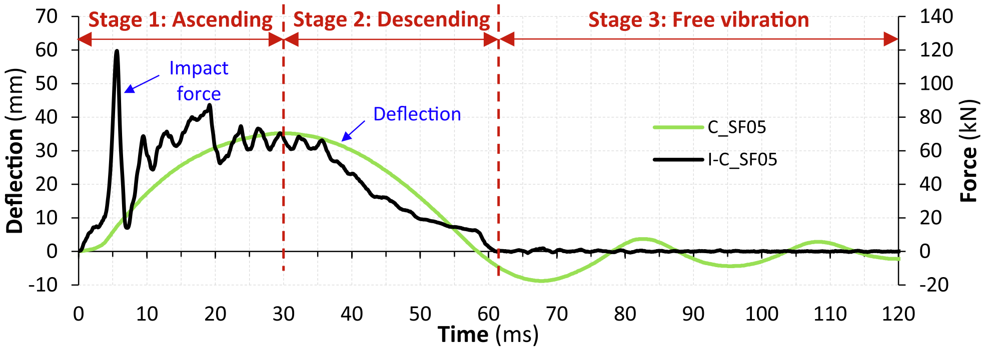

Fig. 9. Stage classification under 40° impact (V_i = 3.09 m/s).

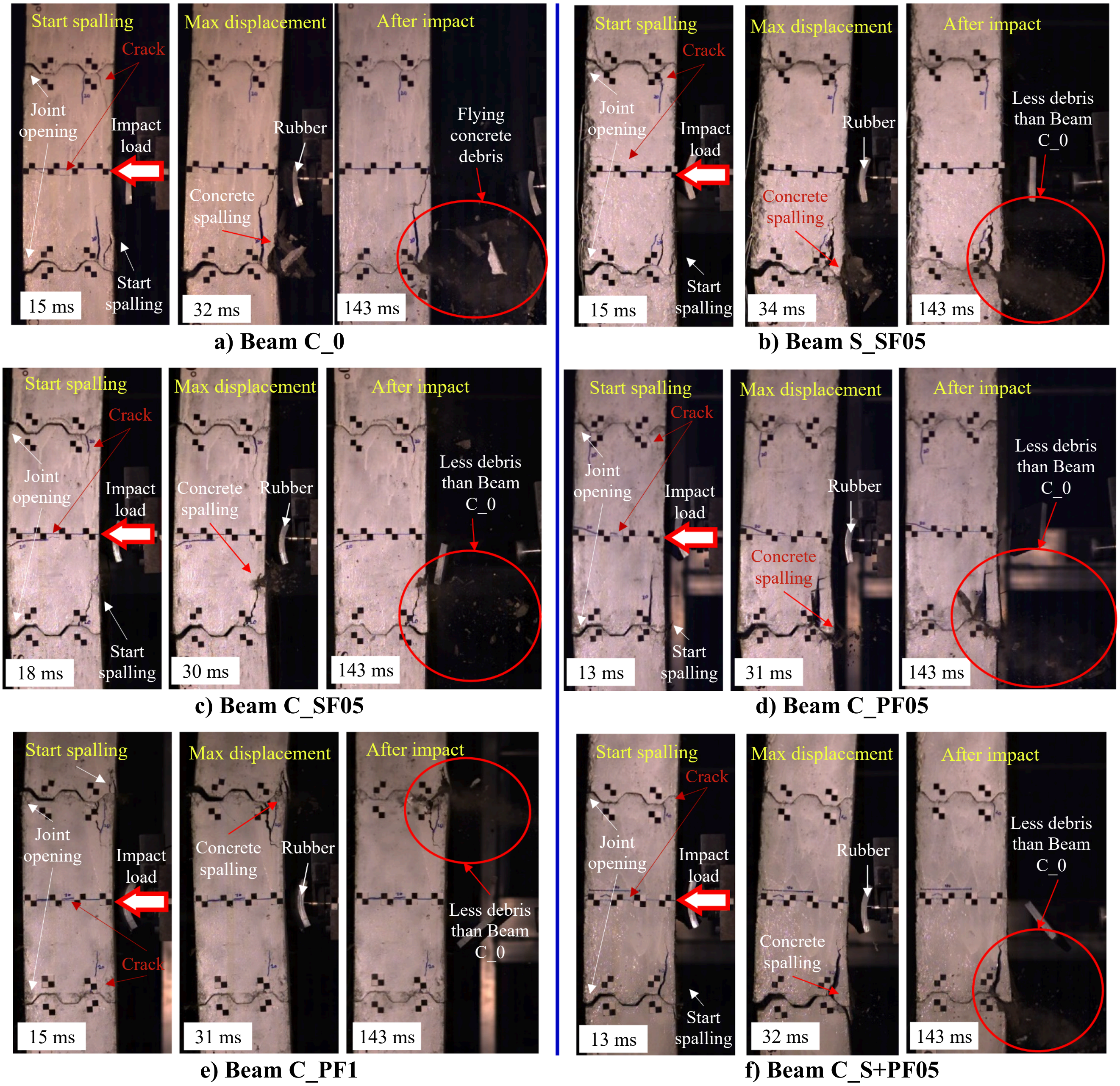

a) Beam C_0

b) Beam S_SF05

c) Beam C_SF05

d) Beam C_PF05

e) Beam C_PF1

f) Beam C_S+PF05

Fig. 10. Damage evolution under 40° impact (V_i = 3.09 m/s).

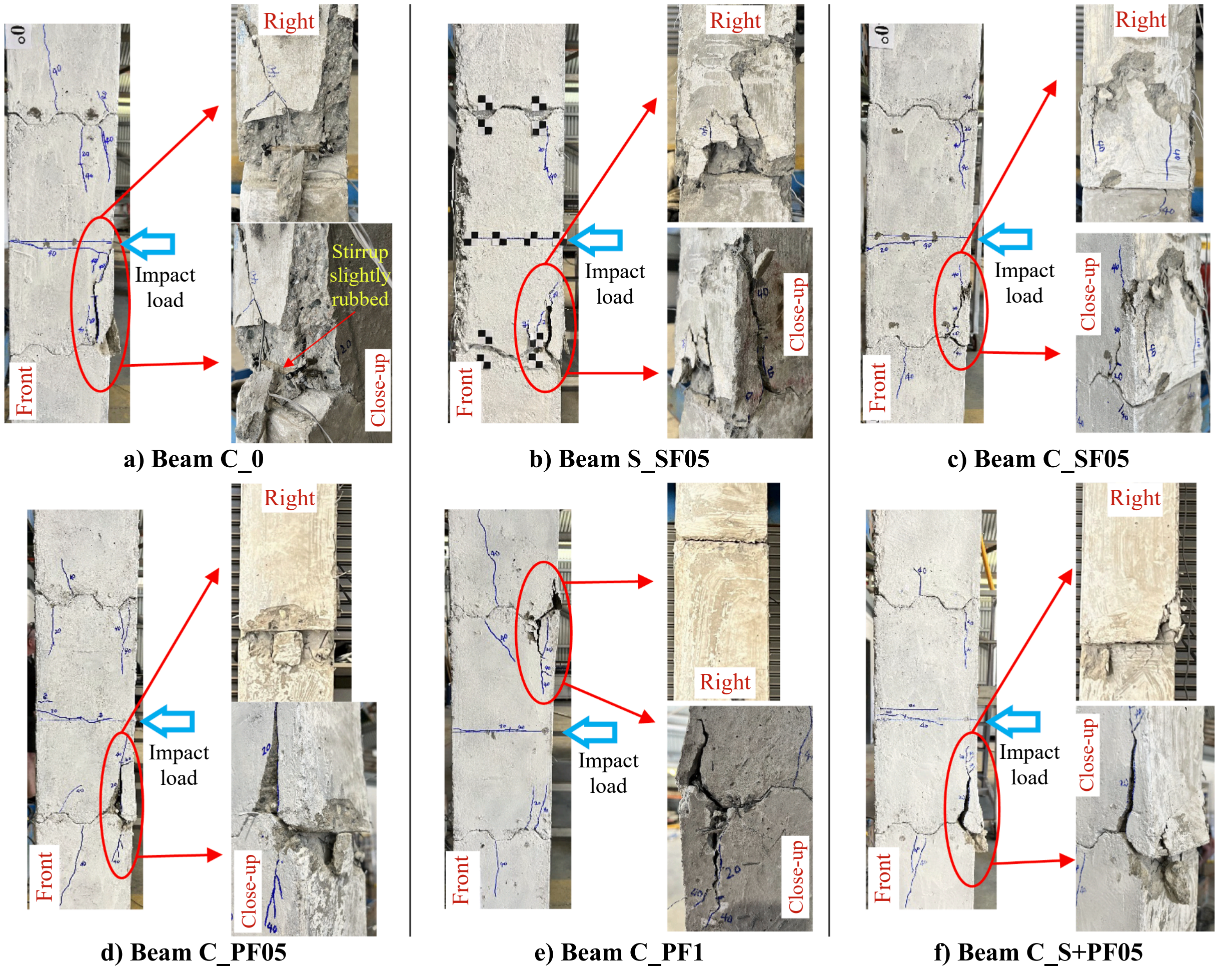

Fig. 11. Beam damage after 40° impact ($V_i = 3.09$ m/s).

crack patterns were virtually the same (see Fig. 6**a**), except that the first crack appeared later, i.e., at around 11 ms, 9 ms, 10 ms and 10 ms for Beams S_SF05, C_PF05, C_PF1 and C_S+PF05, respectively. This is understandable since the concrete tensile strengths of these beams were higher than that of Beam C_0 (Table 3). After the 20° impact ($V_i = 1.52$ m/s), owing to the crack-closing effect of prestressing forces, the bending cracks in the specimens were virtually completely closed and were invisible to the naked eye (see Fig. 6**b**).

The maximum strain in the BFRP reinforcing bar in all the specimens was just 0.08% which was very small (only 4% of the BFRP rupture strain) and thus the BFRP reinforcement was still intact after the 20° impact ($V_i = 1.52$ m/s). No damage to the CFRP and steel tendons was observed in the 20° impact.

3.1.2. *Beam displacement and force in tendon under 20° impact test ($V_i = 1.52$ m/s)*

Fig. 8**a**, **e**, **i** and **m** present the response of the displacement of the specimens under the 20° impact ($V_i = 1.52$ m/s). The displacement response of the PSCB with the CFRP tendon was similar to the PSCB with the steel tendon (Fig. 8**e**). For example, the discrepancy in the maximum displacement between these beams was smaller than 2% (Table 5). The fibres did not have any noticeable effects on the beam displacement under the 20° impact since the displacement–time curves of the PSCBs with various types and dosages of fibres did not exhibit any considerable difference except Beam C_S+PF05 (Fig. 8**a**, **e**, **i** and **m**). This was expected because the 20° impact load ($V_i = 1.52$ m/s) did not cause severe damage or many cracks to the specimens, therefore the fibres were largely not activated to resist the cracks. Owing to the self-centring and closing-crack effects of the prestressing tendon, after the 20° impact ($V_i = 1.52$ m/s), the residual displacement (δ_r) of all the specimens was negligible (Table 5).

The displacement of Beam C_S+PF05 was higher than the reference Beam C_0 with the maximum displacement of the former 15% greater than that of the latter (Table 5). This observation could be attributable to the lower prestressing force (by 16%) of Beam C_S+PF05 compared to Beam C_0, as shown in Table 5. As tendons are the only component resisting tensile stresses in PSCBs, the smaller prestressing force leads to an early opening of the joints in the segmental beam. As observed in [2,4], the stiffness of PSCBs is significantly reduced when joints open. The sooner the stiffness degradation due to the lower prestressing force resulted in the larger displacement of Beam C_S+PF05 compared to Beam C_0. The larger displacement of PSCBs due to the lower prestressing force was also observed in the numerical simulation shown in Fig. A2**b** in the Appendix.

The response of tendon forces under the 20° impact ($V_i = 1.52$ m/s) is shown in Fig. 8**d**, **h**, **l** and **p**. Consistent with the observations from previous investigations on structures prestressed with unbonded tendons under static loads [2,62], the time-tendon force history was analogous with the response of the beam deflection. The tendon force achieved its maximum in Stage 1, coinciding with the peak displacement of the specimen. Then, in Stage 2, the tendon force declined to nearly the original value. The time-tendon force histories of all the specimens during the 20° impact were similar (Fig. 8**d**, **h**, **l** and **p**).

3.1.3. *Impact and reaction forces under 20° impact test ($V_i = 1.52$ m/s)*

Fig. 8**b**, **f**, **j** and **n** present the responses of impact load under the 20°

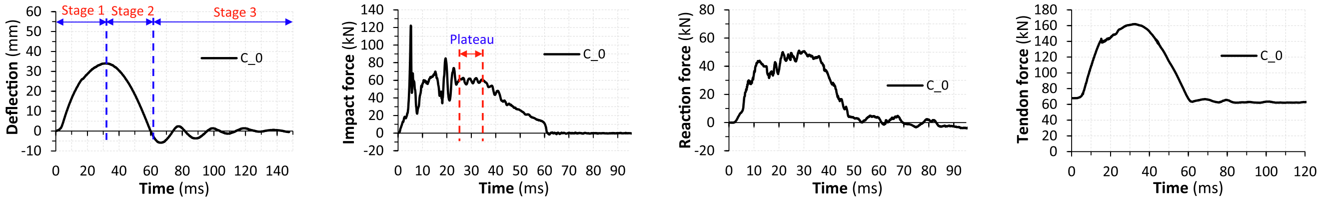

a) Displacement (no fibres) **b)** Impact load (no fibres) **c)** Reaction force (no fibres) **d)** Tendon force (no fibres)

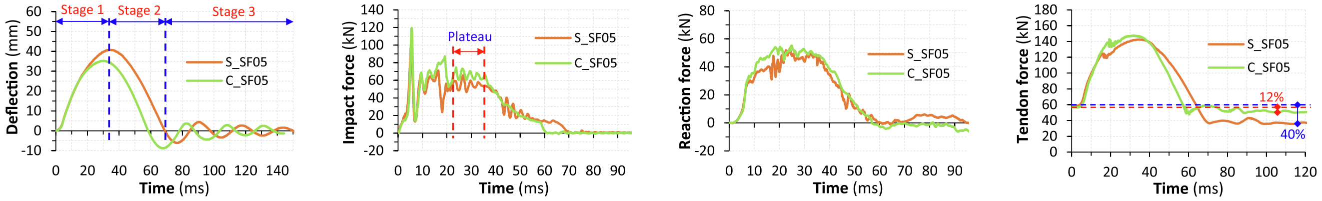

e) Displacement (steel fibres) **f)** Impact load (steel fibres) **g)** Reaction force (steel fibres) **h)** Tendon force (steel fibres)

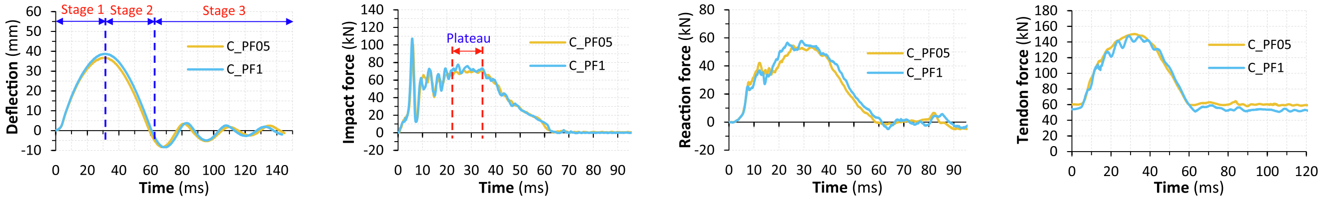

i) Displacement (polypropylene fibres) **j)** Impact load (polypropylene fibres) **k)** Reaction force (polypropylene fibres) **l)** Tendon force (polypropylene fibres)

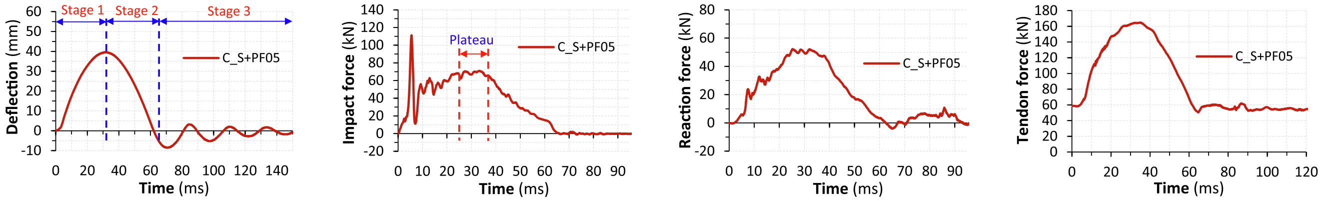

m) Displacement (hybrid fibres) **n)** Impact load (hybrid fibres) **o)** Reaction force (hybrid fibres) **p)** Tendon force (hybrid fibres)

Fig. 12. Responses of displacement, impact load, reaction force and tendon force under the 40° impact ($V_i = 3.09$ m/s).

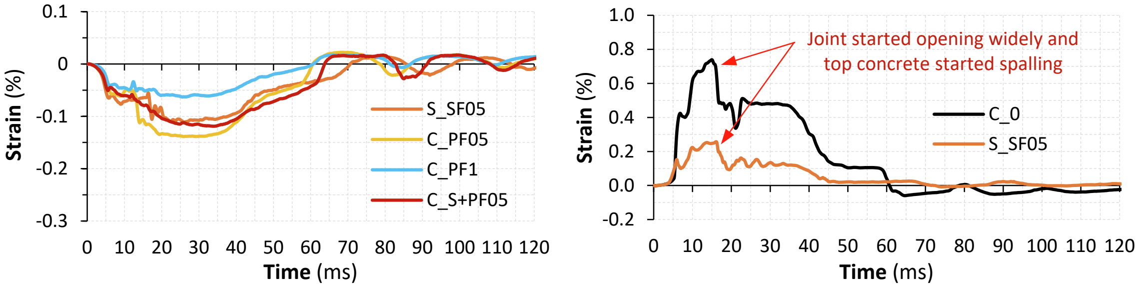

a) Top longitudinal bars b) Bottom longitudinal bars

Fig. 13. Response of longitudinal BFRP bars at midspan under 40° impact ($V_i = 3.09$ m/s).

impact ($V_i = 1.52$ m/s). Owing to several "collisions" between the pendulum and specimen, there were many impact force peaks in Stage 1. During this stage, the impactor and the beam were still in contact while the "collisions" meant the distance between the mass centres fluctuated. The impact load increased when this distance was reduced and vice versa. Fig. 5 shows the stage classification of the impact response. The impact load had a plateau region at the end of Stage 1 (see Fig. 8**b**, **f**, **j** and **n**) when the specimen displacement peaked. The maximum impact force (P_m) and the average impact load in the plateau region (P_{pa}) of the tested beams are summarised in Table 5. Afterwards, the impact load diminished to nil in Stage 2 after the beam and pendulum detached. Rubber pads were used in this study as an interlayer between the pendulum and beam, which decreased the impact load's magnitude and rate and extended the impact load duration as compared to direct contact conditions owing to the rubber's cushion effect. Accordingly, the first impact load peak in this study was not as high as the peak typically witnessed in experiments with direct contact [9]. The beams hit with a high impact velocity tended to have high P_m while the P_{pa} of all the beams with CFRP tendons was similar (Table 5). Although the footage of Beam C_SF05 was lost, it can be deduced that the impact velocity applied on this beam was higher than that of Beam S_SF05 since the impact load of the former was higher than that of the latter (Fig. 8**f**).

Fig. 8**c**, **g**, **k** and **o** show the reaction force response of the specimens under the 20° impact ($V_i = 1.52$ m/s). The reaction force was recorded at only one support because of the limited number of load cells. After the collision with the pendulum, the magnitude of the reaction force increased with a short time delay behind the impact load as typically witnessed in impact tests [25,30,63]. The reaction force rose to the

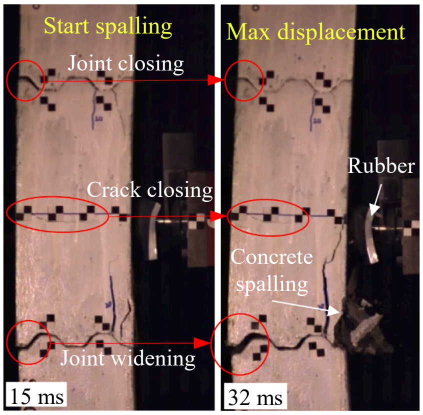

Fig. 14. Deformation of Beam C_0 under 40° impact ($V_i = 3.09$ m/s).

maximum value (R_m in Table 5) at the end of Stage 1 when the specimen attained its peak displacement and the impact load's plateau region. The reaction force was reduced in Stage 2 and fluctuated with a small amplitude in Stage 3 when the beam entered its free-vibration stage. The reaction force response under the 20° impact ($V_i = 1.52$ m/s) of the tested beams was similar.

3.2. Behaviour under 40° impact test ($V_i = 3.09$ m/s)

Table 6 shows the test results of all the beams and Fig. 9 shows a typical time history of displacement and force under the 40° impact ($V_i = 3.09$ m/s). Like the 20° impact ($V_i = 1.52$ m/s), the beam behaviour in the 40° impact test can be divided into three stages including Stage 1 (ascending), Stage 2 (descending) and Stage 3 (free vibration). However, the duration of these stages in the 40° impact was longer than that in the 20° impact, e.g., Stage 1 of the 20° impact lasted roughly 25 ms compared to 32 ms of Stage 1 of the 40° impact. This was expected since the beam was impacted with greater energy and damage caused by the previous 20° impact reduced the beam stiffness and contact stiffness, which also prolonged the interaction between the beam and impactor.

3.2.1. Damage and failure patterns under 40° impact test ($V_i = 3.09$ m/s)

The damage and failure patterns of the tested segmental beams under the 40° impact ($V_i = 3.09$ m/s) are displayed in Fig. 10. The damage and failure patterns of all the beams were similar and mostly happened in Stage 1. The applied 40° impact load first reopened the joints and the cracks (at midspan and around the joints) caused by the previous 20° impact ($V_i = 1.52$ m/s). As the joints opened widely, the shear keys of neighbouring segments were pressed tightly to each other, leading to more cracks emerging from the shear key corners and the top concrete fibres started spalling, as shown in Fig. 10. The excessive joint opening resulted in the failure of the beams, demonstrated via the spallation of the top concrete at the segment joint. The BFRP bars in all the specimens were intact after the 40° impact ($V_i = 3.09$ m/s) except that surface of one BFRP stirrup in Beam C_0 was slightly rubbed by the top concrete spalling off, as shown in Fig. 11**a**. The prestressing CFRP/steel tendons were also undamaged and thus with their self-centring effect, the beams were able to return to approximately their initial positions after the impact (Fig. 10). It is noteworthy that the failure under impact loading of the monolithic beam is normally due to the development of flexural or flexure-shear cracks caused by impact-induced high bending moments and shear forces, as reported in [9]. The overall impact-generated damage to PSCBs is less severe because of the energy absorption capability via the frictional sliding and opening of joints which, however, induced relatively large cracks around the joints and led to the failure of the segmental beam.

Under the high impact load which caused severe damage to the beams, the fibres were activated and played a significant role in reducing the impact-inflicted damage to the beams. The segmental beams failed by the concrete spalling at the joints, causing concrete debris to fly out of the beams at a high speed (see Fig. 10). Flying concrete debris can cause serious injuries to nearby people and damage to surrounding structures. The incorporation of fibres helped control the crack development due to their bridging effect, thereby significantly mitigating the impact-induced damage to the top concrete cover (Fig. 11) and concrete spalling (Fig. 10), as compared to Beam C_0 without fibres. Beam C_0 experienced large pieces of concrete spalled off, exposing the BFRP bars and one stirrup slightly rubbed (Fig. 11**a**). Concrete debris of Beam C_0 flew away during the impact test while damaged concrete pieces of the FRGPC beams were still attached to the beams. With higher modulus, the macro steel fibres (SF) performed better than the macro recycled polypropylene fibres (PF) in reducing the impact-generated damage as demonstrated in Fig. 11**c** vs Fig. 11**d**. Increasing fibre dosage of the macro PF from 0.5% to 1.0% mitigated the damage to the top concrete cover (Fig. 11**d** and e). The adoption of hybrid micro SF and macro PF also slightly reduced the impact-induced damage as compared to the use of solely macro PF, as shown in Fig. 11**f** vs Fig. 11**d**. Furthermore, although having a similar damage pattern, the damage in the beam prestressed with steel tendons (Beam S_SF05) was slightly more severe than the counterpart with CFRP tendons (Beam C_SF05), as shown in Fig. 11**b** and **c**. This could be due to the loss of prestressing force in Beam S_SF05, which is further discussed in the following section.

3.2.2. Beam displacement and force in tendon under 40° impact test ($V_i = 3.09$ m/s)

The beam displacement responses under the 40° impact ($V_i = 3.09$ m/s) are shown in Fig. 12**a**, **e**, **i** and **m**. Although mitigating the damage to the top concrete cover caused by the impact loads, fibres did not have a significant influence on the displacement response of the PSCBs. As shown, the displacement–time histories of all the PSCBs prestressed with CFRP tendons were similar regardless of the types and dosage of fibres. This phenomenon could be explained by the fact that the deformation of the segmental beams was dominantly in the form of joint openings, which led to concrete spalling at the joint and the beam failure, as observed in Fig. 10. In a typical segmental beam, prestressing tendons are the only component resisting joint openings and carrying tensile stresses at joint sections. There were no fibres bridging across the joints to resist the tensile stresses and the fibres only helped control cracks and mitigated concrete spalling on the compression side at the joint section. Therefore, the displacement response of the PSCBs with or without fibres was similar if the same prestressing force was applied. As shown, the peak displacement of the PSCBs with fibres was higher than that of the PSCB without fibres because the initial prestressing force of the former was unexpectedly 19% lower than that of the latter on average (Table 6), leading to stiffness reduction of the beam as explained in Section 3.1.2.

Although being subjected to similar impact energy (similar impact velocity in Table 6) and having a similar damage pattern as mentioned in the previous section under the 40° impact ($V_i = 3.09$ m/s), the PSCB prestressed with steel tendons (Beam S_SF05) had higher displacement as compared to the PSCB with CFRP tendons (Beam C_SF05) (see Fig. 12**c**). This phenomenon was mainly because of the prestress loss in Beam S_SF05, which was evidenced by the residual prestressing force of the steel tendon of only 35 kN, as compared to that in the counterpart Beam C_SF05 (50 kN) (Table 6). This prestress loss was caused by the malfunction of the release system (see Fig. 4**c**) used to release the prestressing force in steel tendons by unscrewing the nut for safe disassembly of the beam after the test. After the 40° impact, it was observed that the nut of the release system was loosened to some extent, resulting in a considerable prestress loss in Beam S_SF05 at 40% by comparing the residual ($F_{p,r}$) vs initial ($F_{p,i}$) tendon forces (see Fig. 12**h** and Table 6). The other test beams with CFRP tendons did not suffer a significant loss in prestressing forces because the release system was not set up in these beams. The reduction in the prestressing force meant that the joints opened earlier and thus the beam stiffness degradation occurred sooner as mentioned in Section 3.1.2, leading to a higher peak displacement of Beam S_SF05, as compared to Beam C_SF05. With higher displacement, the joint in the former opened wider, causing more compressive stresses to the top fibres and hence more damage than the latter as mentioned in the previous section.

The residual displacement (δ_r) of all the specimens under the 40° impact ($V_i = 3.09$ m/s) was small with the value ranging from −0.3 to 0.1 mm (Table 6) owing to the self-centring and closing-crack capabilities of the prestressing tendon.

The response of tendon forces in the PSCBs under the 40° impact test ($V_i = 3.09$ m/s) is presented in Fig. 12**d**, **h**, **l** and **p**. Like the beam displacement response, the force in tendons peaked in Stage 1 when the displacement peaked, then declined to the initial value in Stage 2 and finally oscillated with a small amplitude in Stage 3 (free-vibration stage). Table 6 tabulates the maximum tendon force ($F_{p,m}$) during the 40° impact in each beam. The tendon force during the 40° impact in Beam S_SF05 did not change as much as the other tested beams because of the loss of prestressing force in Beam S_SF05, as mentioned previously. The maximum CFRP tendon force among the tested beams was equal to 54% of the CFRP tendon's tensile strength. This value complied well with the recommendation by a previous study [2] for the maximum allowable tendon force of 75% CFRP tendon's tensile strength to avoid the adverse effect of deformation concentration at the joint. In other words, the CFRP tendon was intact after the 40° impact ($V_i = 3.09$ m/s). The steel tendon was also not damaged since $F_{p,m}$ of Beam S_SF05 (Table 6) was lower than the nominal yield force of the steel tendon, 166 kN. The examination of the beams after the test confirmed there was no damage to the tendons in all the beams.

3.2.3. *Impact and reaction forces under 40° impact test ($V_i = 3.09$ m/s)*

Fig. 12**b**, **f**, **j** and **n** present the responses of impact force under the 40° impact ($V_i = 3.09$ m/s). Fig. 9 illustrates the stage classification of the 40° impact response. The impact force fluctuated significantly and peaked in Stage 1 and at the end of this stage, there was a plateau region of the impact force (see Fig. 12**b**, **f**, **j** and **n**) when the specimen displacement peaked. Table 6 tabulates the maximum impact load (P_m) and the average impact force in the plateau region (P_{pa}). Then, in Stage 2, the impact load declined to nil as the pendulum and beam became detached. Meanwhile, Fig. 12**c**, **g**, **k** and **o** present the time histories of the reaction force. The reaction force response under the 40° impact of all the beams was similar. The reaction force peaked at the end of Stage 1 when the displacement of the specimen peaked and the impact load entered its plateau region. After that, the reaction force diminished in Stage 2 and vibrated with a small amplitude in Stage 3. In comparison with the 20° impact ($V_i = 1.52$ m/s), the impact load's magnitude and duration in the 40° impact ($V_i = 3.09$ m/s) were higher and longer, respectively. Therefore, the impact load impulse in the 40° impact was roughly 2 times higher than that in the 20° impact (Tables 5 and 6). Also, the maximum reaction force (R_m) under the 40° impact was larger than that under the 20° impact by nearly two times (Tables 5 and 6).

The first peak of the impact force depends mainly on the contact stiffness (material properties and contact area) and the impact energy (impact velocity and impactor mass). The contact stiffness and impactor mass were similar for all the test beams. Additionally, the addition of fibres did not considerably affect the concrete modulus and thus the first impact force peak was not expected to vary if the same impact energy was applied, as also observed in the previous studies [25,30]. Accordingly, the first impact force peak, which is also the maximum impact force P_m, was higher in the beam with higher impact velocity, as shown in Tables 5 and 6. The difference in the impact velocity between Beams C-PF0.5 and C-PF1 under the 20° impact was larger than that under the 40° impact. This is the main reason why there was a noticeable difference in the first impact force peak between Beams C-PF0.5 and C-PF1 under the 20° impact, while that difference in the impact force was insignificant in the 40° impact. Concerning the average impact force in the plateau region (P_{pa}), the P_{pa} of the PSCBs with fibres was 15% greater than the P_{pa} of the PSCB without fibres on average (Table 6). The plateau region in the impact force occurred when the specimen attained its maximum displacement and the spallation of the top concrete at the joint occurred as shown in Fig. 10, reducing the contact stiffness of the beam near the striking point. The use of fibres reduced the impact-induced concrete damage as discussed in Section 3.2.1 and thus mitigated the stiffness degradation. Hence, the impact load in the plateau region of the fibre-reinforced specimen was higher compared to the specimen without fibres. The duration (t_d) and the impulse (I) of impact load and the maximum reaction force (R_m) of the FRGPC segmental beams were slightly higher than those of the PSCBs without fibres (Table 6).

The P_{pa} of the PSCB with CFRP tendons (Beam C_SF05) was 18% higher than the P_{pa} of the PSCB with steel tendons (Beam S_SF05) (Table 6). The plateau region in the impact force coincided with the beam maximum displacement, indicating that the global stiffness of the beam was another factor governing P_{pa}. The beam with high stiffness has a high loading resistance and thus attracts more impact forces. The significant prestress loss in Beam S_SF05 resulted in the beam global stiffness reduction, as discussed in Section 3.2.2, and hence reduced the impact force. In addition, the duration of the impact load of Beam S_SF05 was longer than that of Beam C_SF05 (Table 6). The reason might be the smaller global stiffness of the former, which needed more time for the specimen to detach from the pendulum.

3.2.4. *Strain of BFRP bars under 40° impact test ($V_i = 3.09$ m/s)*

Fig. 13 presents the response of the strain of longitudinal BFRP bars at midspan under the 40° impact ($V_i = 3.09$ m/s) (strain gauges' locations are shown in Fig. 2). Due to the malfunction of strain gauges, the BFRP strain in some beams was not available. Similar to the displacement response, the BFRP strain rose to its peak value in Stage 1, declined in Stage 2 and then vibrated with a small amplitude in Stage 3 (see Fig. 9 for the stage classification). In Stages 1 and 2, the bottom and top BFRP longitudinal bars were in compression and tension, respectively. The top BFRP strain in all the specimens was very small with a maximum value of 0.14% (Fig. 13**a**), which is equal to 6.6% of the BFRP rupture strain. Regarding the bottom longitudinal bars, the maximum strain value was 0.74% (Fig. 13**b**), corresponding to 35% of their rupture strains. With their crack-controlling effect, fibres reduced the BFRP strain in the tension side of the beam hence the bottom BFRP strain in Beam S_SF05 was significantly smaller than that of Beam C_0 (Fig. 13**b**). Furthermore, the BFRP stirrups' strain in the tested specimens was also small since the maximum value was 0.024%. Those strain results indicate that the BFRP reinforcement was still intact when the beam failed under the 40° impact ($V_i = 3.09$ m/s).

There was a drop in the bottom BFRP strain in Beams C_0 and S_SF05 at around 16–20 ms, as shown in Fig. 13**b**. When the pendulum collided with the beam, the impact loads deflected the beam, opened the joints and produced high bending moments at midspan, causing transverse cracks (see Fig. 14 at 15 ms) and increasing the strain of the BFRP longitudinal bar at midspan. As the beam deflection increased, one joint opened wide enough to govern the beam deformation, e.g., the bottom joint in Beam C_0 in Fig. 14, resulting in the closing of the other joint and the transverse crack (see Fig. 14 at 32 ms) and the plunge in the bottom BFRP strain. It is noted that this deformation concentration at joints under transverse loading is typical for segmental beams as discussed in [2].

4. Conclusions

This study unveils the impact behaviour of prefabricated segmental concrete beams (PSCBs) made of sustainable and durable materials, i.e., geopolymer concrete (GPC), CFRP tendons and BFRP reinforcement. The beams were struck with three pendulum impact loads with the release angle of 5°, 20° and 40° corresponding to the impact velocity of approximately 0.4 m/s, 1.52 m/s and 3.09 m/s. The effect of dispersed fibres and the performance of PSCBs prestressed with CFRP versus steel tendons are investigated. Based on the experimental data, some conclusions can be reached:

1. The 5° impact load did not cause any visual damage or crack to the tested specimens. The 20° and 40° impact loads induced cracks and severe damage to the PSCBs. Most of the cracks were localised at the joints and emerged from the shear key corners because of stress concentration resulting from joint openings. The PSCBs failed because of the excessive joint opening that resulted in concrete spalling at the joint and concrete debris flying out of the beam.
2. The use of dispersed fibres mitigated the impact-induced damage, delayed crack appearance, decreased reinforcement strain, significantly reduced concrete spalling and the associated stiffness degradation of the beam. Macro steel fibres (SF) performed better than macro recycled polypropylene fibres (PF) in reducing the impact-inflicted concrete damage. Increasing the fibre dosage of the macro PF from 0.5% to 1.0% reduced the concrete damage. Compared to using sole macro PF, applying hybrid micro SF and macro PF slightly reduced the damage.
3. Since the deformation of the segmental beams was governed by joint openings and there was no fibre bridging across the joints, the fibres did not have a significant effect on the displacement response of the PSCBs. The time histories of impact and reaction forces of all the tested beams without or with different types and dosages of fibres were similar.
4. The damage pattern and structural behaviour under impact loading of the segmental beam prestressed with CFRP tendons were similar to those of the beam with conventional steel tendons.
5. The failure of PSCBs was governed by the concrete spalling near the joints owing to joint opening, irrespective of the post-tensioning tendon and reinforcement bar materials. Therefore, CFRP tendons and BFRP reinforcing bars can be adopted to make durable and sustainable precast segmental GPC structures against impact loading.
6. Strengthening the joints would increase the impact-loading resistance capacity of PSCBs. Relevant strengthening measures will be investigated in the future.

CRediT authorship contribution statement

Duong T. Tran: Conceptualization, Methodology, Formal analysis, Investigation, Data curation, Software, Project administration, Writing – original draft, Visualization. **Thong M. Pham:** Conceptualization, Methodology, Writing – review & editing, Supervision. **Hong Hao:** Conceptualization, Methodology, Writing – review & editing, Supervision. **Ngoc San Ha:** Investigation, Writing – review & editing. **Nhi H. Vo:** Investigation, Visualization. **Wensu Chen:** Resources, Writing – review & editing.

Declaration of Competing Interest

The authors declare that they have no known competing financial interests or personal relationships that could have appeared to influence the work reported in this paper.

Data availability

Data will be made available on request.

Acknowledgements

The financial support from the Australian Research Council Laureate Fellowships FL180100196 is acknowledged.

Appendix

Numerical simulation

This study develops a numerical model of the tested beam to further confirm some findings and observations which could not be concluded from the experimental results. However, developing a FE model is not the primary objective of this study and accordingly, only basic information is presented and more information about in-depth FE modelling of prestressed segmental concrete structures can be found in our previous studies [8,9]. The 3D high-fidelity FE model of PSCBs made of GPC and prestressed with CFRP tendons in LS-DYNA is shown in Fig. A1. This is the first study in the open literature that develops a 3D high-fidelity FE model for this type of beam. The concrete, CFRP tendons, rollers, plates, anchors, rubber pad, and impactor were modelled by the default constant-stress solid element in LS-DYNA. The BFRP reinforcing bars and pendulum arm were modelled by the default Hughes-Liu beam element. Based on a convergence investigation, a mesh size of 10 mm was used in this study.

Currently, there is no constitutive material model specifically designed for GPC. The behaviour of GPC is different to OPC due to its high brittleness. However, it has been proven that the K&C concrete model (MAT_072R3) originally intended for OPC can be adapted for GPC [31]. The K&C concrete model has three independent strength surfaces, i.e., the maximum ($\Delta\sigma_m$), yield ($\Delta\sigma_y$) and residual ($\Delta\sigma_r$) strength surfaces, which are expressed in **Eq. (1)** where $j = m$, y and r respectively for the maximum, yield and residual strength surfaces; $p = -(\sigma_{xx} + \sigma_{yy} + \sigma_{zz})/3$ is the pressure with positive stresses in tension and negative stresses in compression; and a_{ij} (i = 0, 1 and 2 and $a_{0r} = 0$) are the parameters defining the three-parameters strength surfaces and calibrated based on the experimental data.

$$\Delta\sigma_j = a_{0j} + \frac{p}{a_{1j} + a_{2j}p} \tag{1}$$

The default parameters of the K&C concrete model and the equation of state (EOS) for OPC with the uniaxial compressive strength $f_c = 40$ MPa are tabulated in Table A1. To reflect the brittleness of GPC, three parameters a_{0y}, a_{1r} and b_1 (compressive damage softening parameter) need to be modified. The values for the GPC with $f_c = 40$ MPa were $a_{0y} = 9.489$, $a_{1r} = 0.3334$ and $b_1 = 0.6$ based on the calibration with test data [31]. To generate the parameters for GPC with a different compressive strength ($f_{c,n}$), the scaling method [64] based on the compressive strength of the previously modelled concrete ($f_{c,o}$) can be adopted. The new strength surfaces $\Delta\sigma_{j,n}$ ($j = m, y$ and r) are expressed in **Eq. (2)** in which $a_{ij,n}$ (i = 0, 1 and 2) are the strength surface parameters for the new concrete; and r is a scaling factor ($=f_{c,n}/f_{c,o}$). The EOS is scaled based on **Eq. (3)** where $EV_{i,n}$ and $EV_{i,n}$, $C_{i,n}$ and C_i, and $K_{i,n}$ and K_i (i = 1 → 10) are respectively the volumetric strains, pressures and bulk moduli of the new and previously modelled concrete. Table A1 shows the parameters for the GPC with $f_c = 53$ MPa. The dynamic-increase-factor (DIF) formulae for concrete in [65] were adopted. Severely distorted concrete elements, which no longer contributed to resisting loads, were discarded once their maximum principal tensile strain exceeded the strain for erosion of 0.4 using the keyword *MAT_ADD_EROSION.

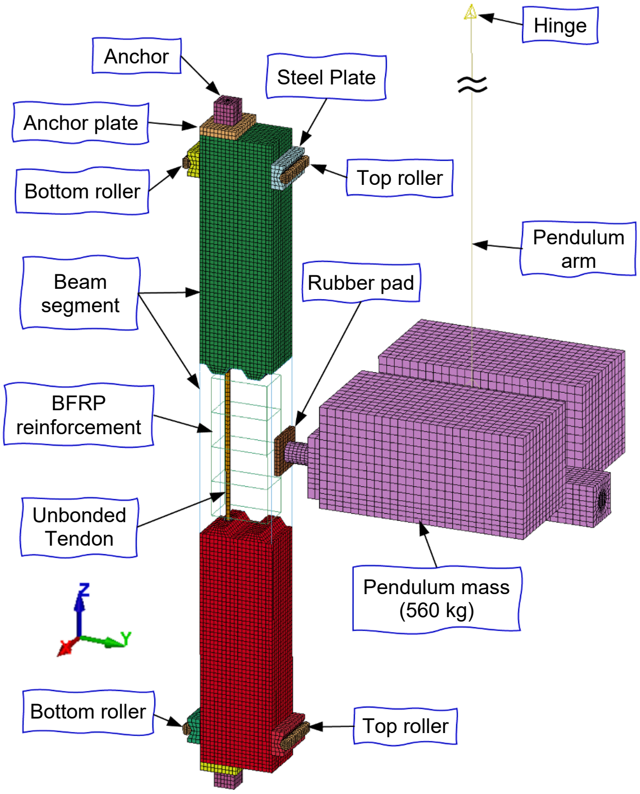

Fig. A1. Numerical model of a prestressed segmental beam.

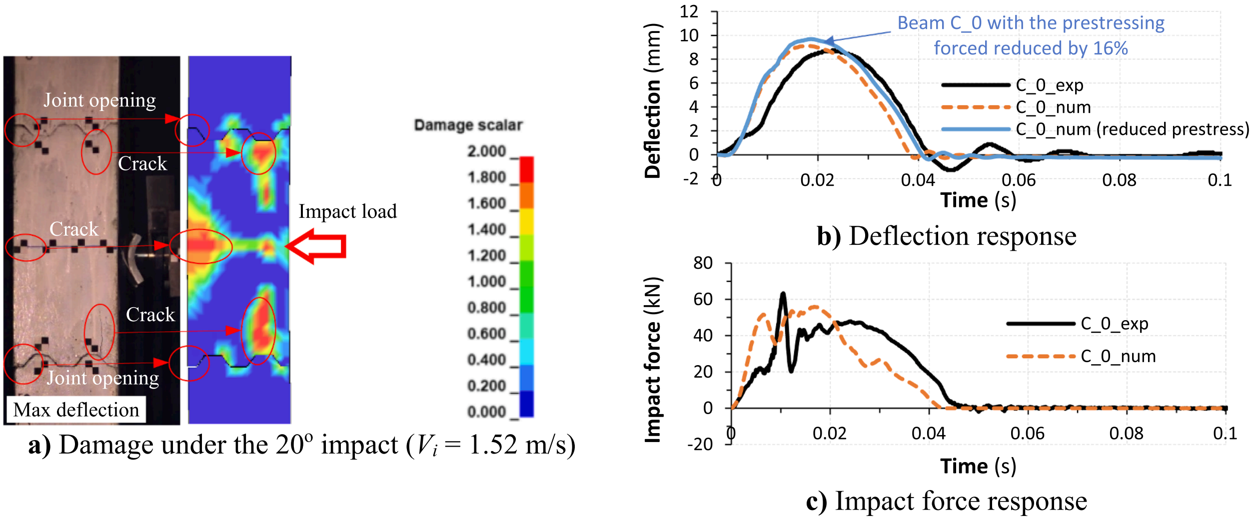

a) Damage under the 20° impact ($V_i = 1.52$ m/s)

b) Deflection response

c) Impact force response

Fig. A2. Validation of the 3D FE model.

$$\begin{aligned}\Delta\sigma_{j,n} &= a_{0j,n} + \frac{p}{a_{1j,n} + a_{2j,n}p}\\ a_{0j,n} &= a_{0j}r\\ a_{1j,n} &= a_{1j}\\ a_{2j,n} &= a_{2j}\Big/r\end{aligned} \tag{2}$$

$$EV_{i,n} = EV_i, \quad C_{i,n} = C_i\sqrt{r}, \quad K_{i,n} = K_i\sqrt{r} \tag{3}$$

Table A2 tabulates the material models and parameters for the other components of the segmental beam. The CFRP tendons were modelled with MAT_054/055 (Enhanced_Composite_Damage) with the parameters based on the manufacturer and the previous studies [2,4,66]. The non-prestressed BFRP reinforcing bars were modelled with MAT_024 (Piecewise_Linear_Plasticity) with the parameters based on the manufacturer. MAT_027 (Mooney-Rivlin_Rubber) was adopted to model the rubber pad with the parameters based on [9]. Keyword *CONTACT_AUTOMATIC_SURFACE_TO_SURFACE was employed to model the contact behaviour. According to the manufacturer, the coefficient of friction

Table A1
Concrete material parameters used in numerical model.

Keywords and Parameters for OPC with f_c = 40 MPa (default parameters)									
***MAT_CONCRETE_DAMAGE_REL3 (072R3)**									
PR	FT	A0 (a_{0m})	A1 (a_{1m})	A2 (a_{2m})	B1	OMEGA	A1F (a_{1r})		
0.19	3.59	11.8237	0.4463	2.0201E-03	1.6	0.5	0.4417		
Slambda	NOUT	EDROP	RSIZE	UCF	LOCWIDTH	NPTS			
100	2	1	0.03937	145	9.1875	0			
lambda1	lambda2	lambda3	lambda4	lambda5	lambda6	lambda7	lambda8		
0	8.00E-06	2.40E-05	4.00E-05	5.60E-05	7.20E-05	8.80E-05	3.20E-04		
lambda9	lambda10	lambda11	lambda12	lambda13	B3	A0Y (a_{0y})	A1Y (a_{1y})		
5.20E-04	5.70E-04	1	10	1.00E + 10	1.15	8.9301	0.6250		
eta1	eta2	eta3	eta4	eta5	eta6	eta7	eta8		
0	0.85	0.97	0.99	1	0.99	0.97	0.5		
eta9	eta10	eta11	eta12	eta13	B2	A2F (a_{2r})	A1Y (a_{2y})		
0.1	0	0	0	0	1.35	2.9561E-03	6.4369E-03		
***EOS_TABULATED_COMPACTION**									
GAMA	E0	V0							
0	0	1							
EV1	EV2	EV3	EV4	EV5	EV6	EV7	EV8	EV9	EV10
0	−0.0015	−0.0043	−0.0101	−0.0305	−0.0513	−0.0726	−0.0943	−0.174	−0.208
C1	C2	C3	C4	C5	C6	C7	C8	C9	C10
0	24.145	52.634	84.510	160.565	242.181	343.591	525.645	3069	4694
T1	T2	T3	T4	T5	T6	T7	T8	T9	T10
0	0	0	0	0	0	0	0	0	0
K1	K2	K3	K4	K5	K6	K7	K8	K9	*K*10
16,097	16,097	16,323	17,139	20,396	23,659	26,910	29,377	66,089	80,477
Keywords and Parameters for GPC with f_c = 53 MPa (this study)									
***MAT_CONCRETE_DAMAGE_REL3 (072R3)**									
PR	FT	A0 (a_{0m})	A1 (a_{1m})	A2 (a_{2m})	B1	OMEGA	A1F (a_{1r})		
0.19	4.14	15.6664	0.4463	1.5246E-03	0.6	0.5	0.3334		
Slambda	NOUT	EDROP	RSIZE	UCF	LOCWIDTH	NPTS			
100	2	1	0.03937	145	30	0			
lambda1	lambda2	lambda3	lambda4	lambda5	lambda6	lambda7	lambda8		
0	8.00E-06	2.40E-05	4.00E-05	5.60E-05	7.20E-05	8.80E-05	3.20E-04		
lambda9	lambda10	lambda11	lambda12	lambda13	B3	A0Y (a_{0y})	A1Y (a_{1y})		
5.20E-04	5.70E-04	1	10	1.00E + 10	1.15	12.5730	0.6250		
eta1	eta2	eta3	eta4	eta5	eta6	eta7	eta8		
0	0.85	0.97	0.99	1	0.99	0.97	0.5		
eta9	eta10	eta11	eta12	eta13	B2	A2F (a_{2r})	A1Y (a_{2y})		
0.1	0	0	0	0	1.35	2.2310E-03	4.8580E-03		
***EOS_TABULATED_COMPACTION**									
GAMA	E0	V0							
0	0	1							
EV1	EV2	EV3	EV4	EV5	EV6	EV7	EV8	EV9	EV10
0	−0.0015	−0.0043	−0.0101	−0.0305	−0.0513	−0.0726	−0.0943	−0.174	−0.208
C1	C2	C3	C4	C5	C6	C7	C8	C9	C10
0	27.793	60.587	97.279	184.824	278.771	395.502	605.063	3533	5403
T1	T2	T3	T4	T5	T6	T7	T8	T9	T10
0	0	0	0	0	0	0	0	0	0
K1	K2	K3	K4	K5	K6	K7	K8	K9	*K*10
18,529	18,529	18,789	19,729	23,477	27,234	30,975	33,815	76,074	92,635

Note: units are metric ton, millimetre, second, N, MPa and N-mm.

(CoF) was 0.3 for the contact between the rubber pad and steel impactor/concrete beam. The CoF were, respectively, 0.7 [2,4] and 0.15 [67] for the contacts between the concrete segments and between the tendon and concrete. Based on the assumption of perfect bonding, the BFRP bar elements were constrained to the concrete medium via the keyword *CONSTRAINED_BEAM_IN_SOLID. Following the test arrangement (see Fig. 4), all the degrees of freedom of the bottom rollers (Fig. A1) were fixed, and each of the top rollers was applied a total force of 13 kN using *LOAD_SEGMENT_SET to simulate the clamping force by the bolts. All the translational and rotational movements of the end node of the pendulum arm were constrained apart from the x-axis rotation to model the hinge support. The effective and convenient method involving *INITIAL_STRESS_SOLID_SET was employed to model the prestressing force in tendons [8,9].

The 3D FE model is verified against the test data of Beam C_0 (see Section 2.2) under the 20° impact ($V_i = 1.52$ m/s). Fig. A2 shows the verification results. Firstly, the FE model could simulate the joint opening and damage caused by the impact load on the beam as shown in Fig. A2**a**. Secondly, the FE model also simulated well the deflection response of the beam when compared with the test result as shown in Fig. A2**b**. Besides, the impact force profile predicted by the FE model was in an acceptable agreement with the test data (see Fig. A2**c**). From the previous results, the 3D high-fidelity FE model developed in this paper can be considered accurate in modelling the impact behaviour of the segmental GPC beam prestressed with CFRP tendons and reinforced with BFRP bars (Beam C_0).

Table A2
Parameters of other materials in the FE model.

Components	Keywords	Parameters	Values
CFRP tendons	*MAT_ENHANCED_COMPOSITE (054/055)	RO (Mass density)	1.580E-09
		EA (Young's modulus)	1.450E+05
		EB and EC	1.030E+04
		PRCB (Poisson's ratio)	0.27
		PRBA and PRCA	0.02
		GAB, GBC and GCA (Shear modulus)	7200
		XC (Longitudinal compressive strength)	1440
		XT (Longitudinal tensile strength)	2450
		YC (Transverse compressive strength)	228
		YT (Transverse tensile strength)	57
		SC (Shear strength)	126
		DFAILT (Max strain for fibre tension)	0.017
		DFAILC (Max strain for fibre compression)	−0.01
BFRP reinforcing bars	*MAT_PIECEWISE_LINEAR_PLASTICITY (024)	RO	2.00E-09
		E	5.50E+04
		PR	0.25
		SIGY	1200
Impactor, rollers, plates, anchors	*MAT_PIECEWISE_LINEAR_PLASTICITY (024)	RO	7.85E-09
		E	2.00E+05
		PR	0.3
		SIGY	300
		ETAN	1102
		FAIL	0.12
Rubber pads	*MAT_MOONEY-RIVLIN_RUBBER (027)	RO	9.50E-10
		PR	0.498
		A	0.5
		B	0.1

Note: units are metric ton, millimetre, second, N, MPa and N-mm.

References

[1] Hao H, Bi K, Chen W, Pham TM, Li J. Towards next generation design of sustainable, durable, multi-hazard resistant, resilient, and smart civil engineering structures. Engineering Structures 2023;277:115477. https://doi.org/10.1016/j.engstruct.2022.115477.

[2] Tran DT, Pham TM, Hao H, Chen W. Numerical Investigation of Flexural Behaviours of Precast Segmental Concrete Beams Internally Post-tensioned with Unbonded FRP Tendons under Monotonic Loading. Engineering Structures 2021; 249:113341. https://doi.org/10.1016/j.engstruct.2021.113341.

[3] Le TD, Pham TM, Hao H, Li H. Behavior of Precast Segmental Concrete Beams Prestressed with External Steel and CFRP Tendons. Journal of Composites for Construction 2020;24(5):04020053. https://doi.org/10.1061/(ASCE)CC.1943-5614.0001059.

[4] Tran DT, Pham TM, Hao H, Chen W. Numerical study on bending response of precast segmental concrete beams externally prestressed with FRP tendons. Engineering Structures 2021;241:112423. https://doi.org/10.1016/j.engstruct.2021.112423.

[5] Vo NH, Pham TM, Hao H, Bi K, Chen W, Ha NS. Blast resistant enhancement of meta-panels using multiple types of resonators. International Journal of Mechanical Sciences 2022;215:106965. https://doi.org/10.1016/j.ijmecsci.2021.106965.

[6] Ha NS, Marundrury SS, Pham TM, Pournasiri E, Shi F, Hao H. Effect of grounded blast furnace slag and rice husk ash on performance of ultra-high-performance concrete (UHPC) subjected to impact loading. Construction and Building Materials 2022;329:127213. https://doi.org/10.1016/j.conbuildmat.2022.127213.

[7] Vo NH, Pham TM, Hao H, Bi K, Chen W. Impact load mitigation of meta-panels with single local resonator. Engineering Structures 2022;265:114528. https://doi.org/10.1016/j.engstruct.2022.114528.

[8] Tran DT, Pham TM, Hao H, Do TV, Tran TT. Blast Behaviour of Precast Segmental vs Monolithic Concrete Beams Prestressed with Unbonded Tendons: A Numerical Investigation. International Journal of Impact Engineering 2023;173:104434. https://doi.org/10.1016/j.ijimpeng.2022.104434.

[9] Tran DT, Pham TM, Hao H, Tran TT, Chen W. Impact Response of Prestressed Prefabricated Segmental and Monolithic Basalt-FRP-Reinforced Geopolymer Concrete Beams. Journal of Composites for Construction 2023;27(5):04023045. https://doi.org/10.1061/JCCOF2.CCENG-4204.

[10] Zhang X, Hao H, Li C. Experimental investigation of the response of precast segmental columns subjected to impact loading. International Journal of Impact Engineering 2016;95:105–24. https://doi.org/10.1016/j.ijimpeng.2016.05.005.

[11] Li J, Hao H, Wu C. Numerical study of precast segmental column under blast loads. Engineering Structures 2017;134:125–37. https://doi.org/10.1016/j.engstruct.2016.12.028.

[12] Do TV, Pham TM, Hao H. Impact Response and Capacity of Precast Concrete Segmental versus Monolithic Bridge Columns. Journal of Bridge Engineering 2019; 24(6):04019050. https://doi.org/10.1061/(ASCE)BE.1943-5592.0001415.

[13] The Australian Government. The Plan to Deliver Net Zero - The Australian Way. Australia: Department of Industry, Science, Energy and Resources; 2021.

[14] Lehne J, Preston F. Making concrete change: Innovation in low-carbon cement and concrete. London: Chatham House; 2018.

[15] Davidovits J. Geopolymers: Inorganic polymeric new materials. Journal of Thermal Analysis and Calorimetry 1991;37(8):1633–56. https://doi.org/10.1007/bf01912193.

[16] Nath P., *Study of fly ash based geopolymer concrete cured in ambient condition*. 2014, Curtin University: WA, Australia.

[17] Sarker PK, Kelly S, Yao Z. Effect of fire exposure on cracking, spalling and residual strength of fly ash geopolymer concrete. Materials and Design 2014;63:584–92. https://doi.org/10.1016/j.matdes.2014.06.059.

[18] Okoye FN, Prakash S, Singh NB. Durability of fly ash based geopolymer concrete in the presence of silica fume. Journal of Cleaner Production 2017;149:1062–7. https://doi.org/10.1016/j.jclepro.2017.02.176.

[19] Sarker PK, Haque R, Ramgolam KV. Fracture behaviour of heat cured fly ash based geopolymer concrete. Materials and Design 2013;44:580–6. https://doi.org/10.1016/j.matdes.2012.08.005.

[20] Tran TT, Pham TM, Hao H. Experimental and analytical investigation on flexural behaviour of ambient cured geopolymer concrete beams reinforced with steel fibers. Engineering Structures 2019;200:109707. https://doi.org/10.1016/j.engstruct.2019.109707.

[21] Bhutta A, Borges PHR, Zanotti C, Farooq M, Banthia N. Flexural behavior of geopolymer composites reinforced with steel and polypropylene macro fibers. Cement and Concrete Composites 2017;80:31–40. https://doi.org/10.1016/j.cemconcomp.2016.11.014.

[22] Tran TT, Pham TM, Hao H. Effect of hybrid fibers on shear behaviour of geopolymer concrete beams reinforced by basalt fiber reinforced polymer (BFRP) bars without stirrups. Composite Structures 2020;243:112236. https://doi.org/10.1016/j.compstruct.2020.112236.

[23] Shi F, Pham TM, Hao H, Hao Y. Post-cracking behaviour of basalt and macro polypropylene hybrid fibre reinforced concrete with different compressive strengths. Construction and Building Materials 2020;262:120108. https://doi.org/10.1016/j.conbuildmat.2020.120108.

[24] Do-Dai T, Tran DT, Nguyen-Minh L. Effect of fiber amount and stirrup ratio on shear resistance of steel fiber reinforced concrete deep beams. Journal of Science and Technology in Civil Engineering (STCE) - HUCE 2021;15(2):1–13. https://doi.org/10.31814/stce.nuce2021-15(2)-01.

[25] Tran TT, Pham TM, Huang Z, Chen W, Ngo TT, Hao H, et al. Effect of fibre reinforcements on shear capacity of geopolymer concrete beams subjected to impact load. International Journal of Impact Engineering 2022;159:104056. https://doi.org/10.1016/j.ijimpeng.2021.104056.

[26] Do-Dai T, Chu-Van T, Tran DT, Nassif AY, Nguyen-Minh L. Efficacy of CFRP/BFRP laminates in flexurally strengthening of concrete beams with corroded reinforcement. Journal of Building Engineering 2022;53:104606. https://doi.org/10.1016/j.jobe.2022.104606.

[27] Huynh-Xuan T, Do-Dai T, Ngo-Huu C, Pham TM, Nguyen-Minh L. Effect of corroded reinforcement on capacity of square reinforced concrete columns confined with FRP sheets under eccentric loads. Engineering Structures 2023;283:115821. https://doi.org/10.1016/j.engstruct.2023.115821.

[28] Fan X, Zhang M. Experimental study on flexural behaviour of inorganic polymer concrete beams reinforced with basalt rebar. Composites Part B Engineering 2016;93:174–83. https://doi.org/10.1016/j.compositesb.2016.03.021.

[29] Rashid K, Li X, Xie Y, Deng J, Zhang F. Cracking behavior of geopolymer concrete beams reinforced with steel and fiber reinforced polymer bars under flexural load. Composites Part B Engineering 2020;186:107777. https://doi.org/10.1016/j.compositesb.2020.107777.

[30] Tran TT, Pham TM, Huang Z, Chen W, Hao H, Elchalakani M. Impact response of fibre reinforced geopolymer concrete beams with BFRP bars and stirrups. Engineering Structures 2021;231:111785. https://doi.org/10.1016/j.engstruct.2020.111785.

[31] Huang Z, Chen W, Hao H, Chen Z, Pham TM, Tran TT, et al. Flexural behaviour of ambient cured geopolymer concrete beams reinforced with BFRP bars under static and impact loads. Composite Structures 2021;261:113282. https://doi.org/10.1016/j.compstruct.2020.113282.

[32] Ngo TT, Pham TM, Hao H, Chen W, Ha NS. Proposed new dry and hybrid concrete joints with GFRP bolts and GFRP reinforcement under cyclic loading: Testing and analysis. Journal of Building Engineering 2022;49:104033. https://doi.org/10.1016/j.jobe.2022.104033.

[33] Bekaert. *Dramix 3D Steel Fibres*. https://www.bekaert.com/en/.

[34] BarChip Inc. *BarChip R50 Recycled Polypropylene Fibres*. https://barchip.com/.

[35] Subote. *Copper-coated Steel Fibres*.

[36] Balanji EKZ, Sheikh MN, Hadi MNS. Behaviour of high strength concrete reinforced with different types of steel fibres. Australian Journal of Structural Engineering 2017;18(4):254–61. https://doi.org/10.1080/13287982.2017.1396871.

[37] Zhang H, Sarker PK, Wang Q, He B, Jiang Z. Strength and toughness of ambient-cured geopolymer concrete containing virgin and recycled fibres in mono and hybrid combinations. Construction and Building Materials 2021;304:124649. https://doi.org/10.1016/j.conbuildmat.2021.124649.

[38] BarChip Inc. *Batching and Mixing Guide for Barchip's Synthetic Fiber Reinforcement*. https://barchip.com/epc-batching-and-mixing-guide/.

[39] Bekaert.. Recommendations for handling, dosing and mixing. Mariettta, GA: Bekaert 2012.

[40] Standards Australia. *Methods of testing concrete - Method 9: Compressive strength tests - Concrete, mortar and grout specimens. AS 1012.9:2014*. Sydney, NSW: Standards Australia; 2014.

[41] Standards Australia. *Methods of testing concrete - Method 8.1: Method for making and curing concrete - Compression and indirect tensile test specimens. AS 1012.8.1:2014*. Sydney, NSW: Standards Australia; 2014.

[42] Behfarnia K, Behravan A. Application of high performance polypropylene fibers in concrete lining of water tunnels. Materials and Design 2014;55:274–9. https://doi.org/10.1016/j.matdes.2013.09.075.

[43] Astm. Standard Specification for Low-Relaxation, Seven-Wire Steel Strand for Prestressed Concrete. ASTM A416/A416M-18. West Conshohocken, PA: ASTM International; 2018.

[44] Dextra Group. *Carbon fibre-reinforced polymer tendons*. GuangDong, China: Dextra Building Products (Guangdong) Co., Ltd.

[45] Green Material Valley Technology. *Basalt fiber-reinforced polymer composite bar*. Nanjing, China: Jiangsu Green Material Valley New Material Technology Development Co., Ltd.

[46] Cotsovos DM, Stathopoulos ND, Zeris CA. Behavior of RC Beams Subjected to High Rates of Concentrated Loading. Journal of Structural Engineering 2008;134(12):1839–51. https://doi.org/10.1061/(ASCE)0733-9445(2008)134:12(1839).

[47] Nagata M, Beppu M, Ichino H, Matsuzawa R. A fundamental investigation of reinforced concrete beams subjected to close-in explosion. International Journal of Protective Structures 2018;9(2):174–98. https://doi.org/10.1177/2041419617716483.

[48] Dang TD, Tran DT, Nguyen-Minh L, Nassif AY. Shear resistant capacity of steel fibres reinforced concrete deep beams: An experimental investigation and a new prediction model. Structures 2021;33:2284–300. https://doi.org/10.1016/j.istruc.2021.05.091.

[49] Nguyen-Minh L, Vo-Le D, Tran-Thanh D, Pham TM, Ho-Huu C, Rovňák M. Shear capacity of unbonded post-tensioned concrete T-beams strengthened with CFRP and GFRP U-wraps. Composite Structures 2018;184:1011–29. https://doi.org/10.1016/j.compstruct.2017.10.072.

[50] Truong QPT, Phan-Vu P, Tran-Thanh D, Dang TD, Nguyen-Minh L. In: Flexural Behavior of Unbonded Post-Tensioned Concrete T-Beams Externally Bonded With CFRP Sheets Under Static Loading. Phu Quoc, Vietnam: Springer; 2018. https://doi.org/10.1007/978-981-10-7149-2_19.

[51] Phan-Vu P., Tran D.T., Ngo-Huu C., Dang T.D., and Nguyen-Minh L. *Flexural behaviour of unbonded post-tensioned concrete T-beams strengthened with CFRP sheets under repeated loading.* In *Proceedings of the 7th International Conference on Protection of Structures against Hazards (PSH2018)*. 2018. Hanoi, Vietnam: CI-Premier Pte Ltd, Singapore.

[52] Aci. Building Code Requirements for Structural Concrete (ACI 318–19) and Commentary. Farmington Hills, MI: American Concrete Institute (ACI); 2019.

[53] Tran DT, Phan-Vu P, Pham TM, Dang TD, Nguyen-Minh L. Repeated and Post-Repeated Flexural Behavior of Unbonded Post-Tensioned Concrete T-Beams Strengthened with CFRP Sheets. Journal of Composites for Construction 2020;24(2):04019064. https://doi.org/10.1061/(ASCE)CC.1943-5614.0000996.

[54] Phan-Vu P, Tran DT, Pham TM, Dang TD, Ngo-Huu C, Nguyen-Minh L. Distinguished bond behaviour of CFRP sheets in unbonded post-tensioned reinforced concrete beams versus single-lap shear tests. Engineering Structures 2021;234:111794. https://doi.org/10.1016/j.engstruct.2020.111794.

[55] Vo-Le D, Tran DT, Pham TM, Ho-Huu C, Nguyen-Minh L. Re-evaluation of shear contribution of CFRP and GFRP sheets in concrete beams post-tensioned with unbonded tendons. Engineering Structures 2022;259:114173. https://doi.org/10.1016/j.engstruct.2022.114173.

[56] Zeck UI. Joints in large panel precast concrete structures. Cambridge, Massachusetts: Massachusetts Institute of Technology; 1976.

[57] Koseki K, Breen JE. Exploratory study of shear strength of joints for precast segmental bridges. Austin, Texas: The University of Texas at Austin; 1983.

[58] Aashto. Guide Specifications for Design and Construction of Segmental Concrete Bridges, 2nd Edition, with 2003 Interim Revisions. Washington, DC: American Association of State Highway and Transportation Officials (AASHTO); 2003.

[59] Aci. Guide for the Design and Construction of Structural Concrete Reinforced with Fiber-Reinforced Polymer (FRP) Bars. Farmington Hills, Michigan: American Concrete Institute (ACI); 2015.

[60] Ireland DR. In: Procedures and Problems Associated with Reliable Control of the Instrumented Impact Test. West Conshohocken, PA: ASTM International; 1974. p. 3–29.

[61] Pham TM, Chen W, Hao H. Review on impact response of reinforced concrete beams: Contemporary understanding and unsolved problems. Advances in Structural Engineering 2021;1369433221997716. https://doi.org/10.1177/1369433221997716.

[62] Nguyen-Minh L, Phan-Vu P, Tran-Thanh D, Phuong Thi Truong Q, Pham TM, Ngo-Huu C, et al. Flexural-strengthening efficiency of CFRP sheets for unbonded post-tensioned concrete T-beams. Engineering Structures 2018;166:1–15. https://doi.org/10.1016/j.engstruct.2018.03.065.

[63] Pham TM, Hao H. Impact Behavior of FRP-Strengthened RC Beams without Stirrups. Journal of Composites for Construction 2016;20(4):04016011. https://doi.org/10.1061/(ASCE)CC.1943-5614.0000671.

[64] Malvar LJ, Crawford JE, Wesevich JW, Simons D. A plasticity concrete material model for DYNA3D. International Journal of Impact Engineering 1997;19(9):847–73. https://doi.org/10.1016/S0734-743X(97)00023-7.

[65] Hao Y, Hao H. Influence of the concrete DIF model on the numerical predictions of RC wall responses to blast loadings. Engineering Structures 2014;73:24–38. https://doi.org/10.1016/j.engstruct.2014.04.042.

[66] Chan S, Fawaz Z, Behdinan K, Amid R. Ballistic limit prediction using a numerical model with progressive damage capability. Composite Structures 2007;77(4):466–74. https://doi.org/10.1016/j.compstruct.2005.08.022.

[67] Institute P-T. Post-Tensioning Manual. Sixth edition. Phoenix, Arizona: Post-Tensioning Institute; 2006.